



TechBriefs

National Aeronautics and
Space Administration



Electronic Components and Circuits



Electronic Systems



Physical Sciences



Materials



Computer Programs



Mechanics



Machinery



Fabrication Technology



Mathematics and Information Sciences



Life Sciences

INTRODUCTION

Tech Briefs are short announcements of innovations originating from research and development activities of the National Aeronautics and Space Administration. They emphasize information considered likely to be transferable across industrial, regional, or disciplinary lines and are issued to encourage commercial application.

Availability of NASA Tech Briefs and TSPs

Requests for individual Tech Briefs or for Technical Support Packages (TSPs) announced herein should be addressed to

National Technology Transfer Center

Telephone No. (800) 678-6882 or via World Wide Web at www2.nttc.edu/leads/

Please reference the control numbers appearing at the end of each Tech Brief. Information on NASA's Commercial Technology Team, its documents, and services is also available at the same facility or on the World Wide Web at www.nctn.hq.nasa.gov.

Commercial Technology Offices and Patent Counsels are located at NASA field centers to provide technology-transfer access to industrial users. Inquiries can be made by contacting NASA field centers and program offices listed below.

NASA Field Centers and Program Offices

Ames Research Center

Carolina Blake
(650) 604-1754 or
cblake@mail.arc.nasa.gov

Dryden Flight Research Center

Jenny Baer-Riedhart
(661) 276-3689 or
jenny.baer-riedhart@dfrc.nasa.gov

Goddard Space Flight Center

George Alcorn
(301) 286-5810 or
galcorn@gsfc.nasa.gov

Jet Propulsion Laboratory

Merle McKenzie
(818) 354-2577 or
merle.mckenzie@jpl.nasa.gov

Johnson Space Center

Hank Davis
(281) 483-0474 or
henry.l.davis@jsc.nasa.gov

John F. Kennedy Space Center

Jim Aliberti
(321) 867-6224 or
Jim.Aliberti-1@ksc.nasa.gov

Langley Research Center

Sam Morello
(757) 864-6005 or
s.a.morello@larc.nasa.gov

Glenn Research Center

Larry Viterna
(216) 433-3484 or
cto@grc.nasa.gov

George C. Marshall Space Flight Center

Sally Little
(256) 544-4266 or
sally.little@msfc.nasa.gov

John C. Stennis Space Center

Kirk Sharp
(228) 688-1929 or
technology@ssc.nasa.gov

NASA Program Offices

At NASA Headquarters there are seven major program offices that develop and oversee technology projects of potential interest to industry:

Carl Ray

Small Business Innovation
Research Program (SBIR) &
Small Business Technology
Transfer Program (STTR)
(202) 358-4652 or
cray@mail.hq.nasa.gov

Dr. Robert Norwood

Office of Commercial Technology
(Code RW)
(202) 358-2320 or
rnorwood@mail.hq.nasa.gov

John Mankins

Office of Space Flight (Code 14P)
(202) 358-4659 or
jmankins@mail.hq.nasa.gov

Terry Hertz

Office of Aero-Space Technology
(Code RS)
(202) 358-4626 or
thertz@mail.hq.nasa.gov

Glen Mucklow

Office of Space Sciences
(Code SM)
(202) 358-2235 or
gmucklow@mail.hq.nasa.gov

Roger Crouch

Office of Microgravity Science
Applications (Code U)
(202) 358-0689 or
rcrouch@hq.nasa.gov

Granville Paules

Office of Mission to Planet Earth
(Code Y)
(202) 358-0706 or
gpaules@mtpe.hq.nasa.gov



National Aeronautics and
Space Administration

TechBriefs

December 2000
00-12

5	Electronic Components and Circuits	
---	------------------------------------	---

11	Electronic Systems	
----	--------------------	---

19	Physical Sciences	
----	-------------------	---

27	Computer Programs	
----	-------------------	---

31	Mechanics	
----	-----------	--

35	Machinery	
----	-----------	---

39	Fabrication Technology	
----	------------------------	---

43	Mathematics and Information Sciences	
----	--------------------------------------	---

This document was prepared under the sponsorship of the National Aeronautics and Space Administration. Neither the United States Government nor any person acting on behalf of the United States Government assumes any liability resulting from the use of the information contained in this document, or warrants that such use will be free from privately owned rights.

4

BLANK PAGE



Electronic Components and Circuits

Hardware, Techniques, and Processes

- 7 Silicon Carbide npnp Thyristors
- 8 GA Synthesis of Circuits Using a Linear Representation
- 9 Generating Electric Power From Alpha-Particle Sources
- 9 High-Performance Photodetector Circuit for Doppler Lidar

Silicon Carbide npnp Thyristors

These devices can be operated at temperatures up to 350 °C.

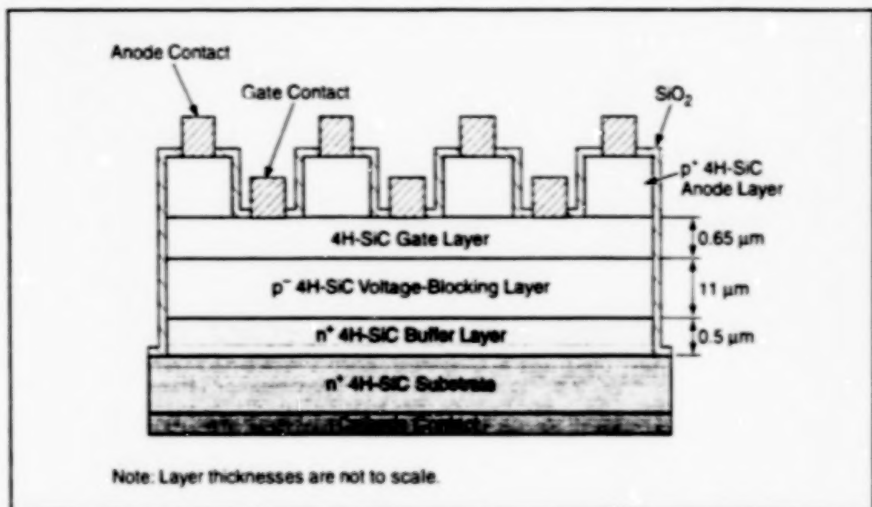
John H. Glenn Research Center,
Cleveland, Ohio

Thyristors (semiconductor controlled rectifiers) made from silicon carbide have been fabricated and tested as prototypes of power-switching devices capable of operating at temperatures up to 350 °C. The highest-voltage-rated of these thyristors are capable of blocking current at forward or reverse bias as large as 900 V, and can sustain forward current as large as 2 A with a forward potential drop of -3.9 V. The highest-power-rated of these thyristors (which are also the highest-power-rated SiC thyristors reported thus far) can block current at a forward or reverse bias of 700 V and can sustain an "on" current of 6 A at a forward potential drop of -3.67 V. The highest-current-rated of these thyristors can block current at a forward or reverse bias of 400 V and can sustain an "on" current of 10 A.

These thyristors feature epitaxial n- and p-doped layers of 4H SiC in the sequence npnp starting on the substrate; this structure (see figure) stands in contrast to the npnp structure of common silicon thyristors. The fabrication of the high-quality crystalline structures needed in these layers has been made possible by advances in growth of crystals, epitaxial growth of thin films, doping by both *in situ* and ion-implantation techniques, oxidation, formation of electrical contacts, and other techniques involved in the fabrication of electronic devices.

The reasons for choosing the npnp structure and for choosing the 4H polytype of SiC (instead of choosing the more common 6H polytype) are the following:

- The npnp structure was adopted to avoid the very high resistances of typical p-doped SiC substrates. In the research that led to the development of the present thyristors, the resistances of p-doped substrates were found to dominate the characteristics of npnp SiC thyristors.
- It was found in this research that the electron mobilities along the electrical-current paths in 4H-SiC thyristors of the present 4-layer configuration are about 10x those of similar thyristors made from 6H-SiC. Thus, 4H-SiC offers the potential to achieve greater current densities.
- It was also found in this research that the defect densities of the 4H-SiC layers (which are formed by epitaxy) are much



This Cross Section (not to scale) shows the npnp-layer structure of a representative thyristor of the present type. The n⁺, p⁻, n⁻, and p⁺-doped 4H-SiC layers are formed by epitaxy on the n⁺ 4H-SiC substrate, which is cut at an angle of 8° off axis.

smaller when substrates cut at large off-axis angles are used. 6H-SiC substrates are typically cut at 3.5° off axis. However, it was found that when 4H-SiC substrates are cut at 3.5° off axis, large numbers of 3C-SiC inclusions are observed in the epilayers. It was found that the 3C-SiC inclusions can be eliminated by growing on 4H-SiC substrates cut at 8° off axis. The highest-power-rated thyristors were found to be achievable only by use of 8°-off-axis-cut 4H-SiC substrates.

Some of these thyristors rated at voltages >400 V and currents >5 A have been characterized at temperatures up to 350 °C. The forward voltage drop at a current of 5 A was found to decrease monotonically from 3.91 V at 27 °C to 3.18 V at 350 °C. The leakage current density at a reverse bias of 400 V was found to increase from about 10⁻⁶ A/cm² at room temperature to 9 × 10⁻³ A/cm² at 350 °C. Even at 350 °C, the ratio between the "on" current and the leakage ("off") current was found to be about 10³, which should be an acceptable ratio for a power device.

Some of the thyristors were packaged, then stored for 1,000 hours at 350 °C. While many of these thyristors failed, about 25 percent survived the 1,000 hours without significant degradation.

The npnp 4H-SiC thyristors were found to be capable of switching at very high speeds. For example, a 600-V, 2-A device

was tested to determine its maximum repetition rate for a peak current of 7 A pulsed at a 20-percent duty cycle. It was found that the gate pulse could be repeated after a period of only 4 μs, corresponding to a maximum pulse-repetition frequency of 250 kHz. This speed exceeds the speed of the fastest inverter-grade silicon thyristors.

Two other important parameters for a thyristor are (1) the maximum rate of increase of forward applied voltage that can be applied before the thyristor latches on and (2) the time taken to achieve a high forward current density. The 4H-SiC thyristors tested showed no turn-on even when forward bias was ramped up at a rate of 900 V/μs. Measurements in pulsed operation showed that it took between 3 and 5 nanoseconds for these devices to start carrying currents at densities of 2,800 A/cm².

This work was done by John Palmour and Calvin H. Cartier, Jr., of Cree Research, Inc., for Glenn Research Center. Further information is contained in a TSP [see page 1].

Inquiries concerning rights for the commercial use of this invention should be addressed to NASA Glenn Research Center, Commercial Technology Office, Attn: Steve Fedor, Mail Stop 4-8, 21000 Brookpark Road, Cleveland, Ohio 44135. Refer to LEW-16750.

GA Synthesis of Circuits Using a Linear Representation

The procedure for designing many practical circuits can be partly automated.

Ames Research Center,
Moffett Field, California

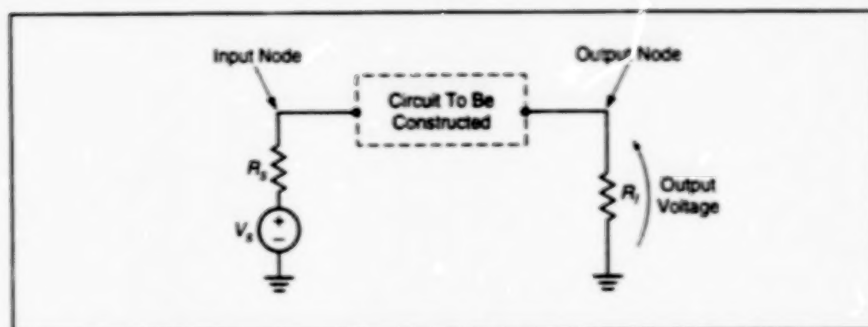


Figure 1. A Circuit Is Constructed between fixed input and output terminals. The input source voltage V_s , source resistance R_s , and load resistance R_l are specified in advance.

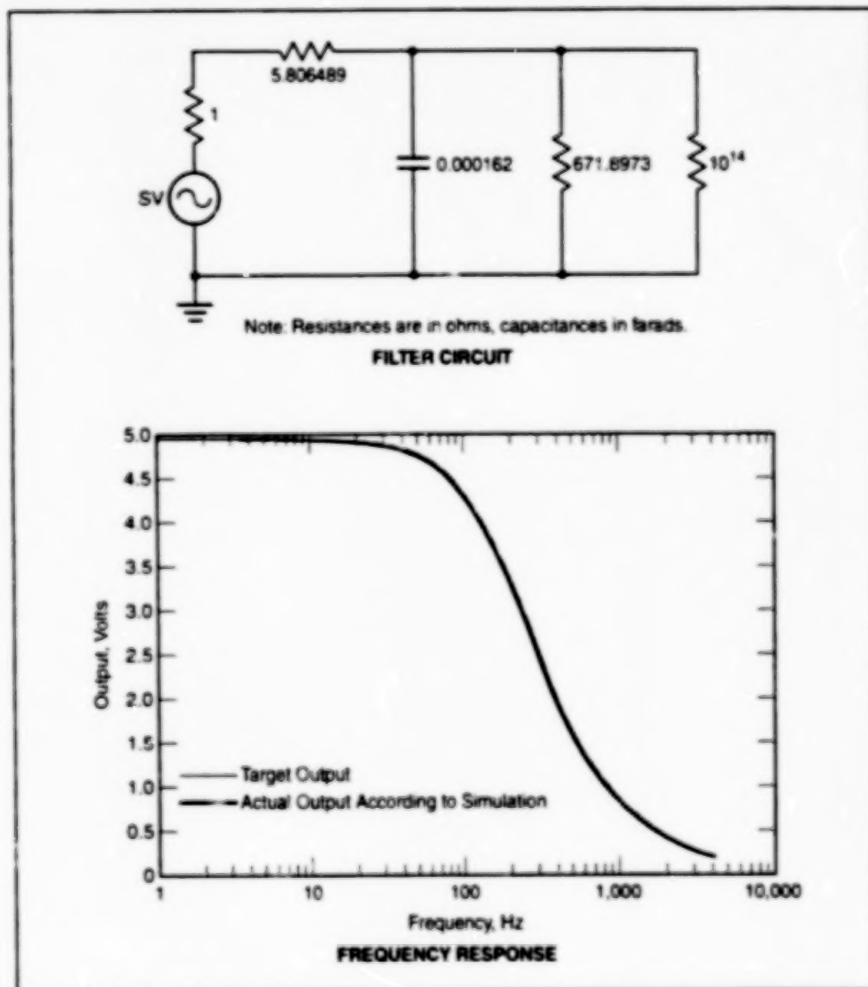


Figure 2. This Low-Pass Filter for an electronic stethoscope was synthesized by the method described in the text. The simulated frequency response of the circuit is nearly identical to the target frequency response.

A method of automated synthesis of electronic circuits involves the use of a linear (as defined below) genome representation of circuit elements and of connections among them, plus a relatively simple unfolding technique, in conjunc-

tion with a genetic algorithm (GA). The method differs from most other GA-based circuit-synthesis methods in that the topology of a circuit, the number of its components, and the types and values of its components (e.g., induc-

tances, capacitances, and resistances) are all made to evolve by use of the GA.

The linear genome representation is a list of byte codes. The unfolding process is essentially an algorithm in which the byte codes are interpreted to construct a mathematical model of a circuit. In each step of the process, the algorithm starts at one node of the circuit (called the "active node"), proceeds to another node, and connects the two nodes with a component, as instructed by a byte code. The byte code for each component includes (1) an opcode, which specifies the type of component and the identity of the node to which the far end of the component is to be connected, and (2) bytes that specify the value of the component.

The unfolding process begins at a fixed input node and ends at a fixed output node (see Figure 1). In a given step of the process, the far end of a component can be connected to a node that was created previously (e.g., to input, output, or ground), or to a newly created node. When a new node is created, the new node becomes the starting point for the next step. An exception to the unfolding process as described thus far is made for the last component in the list: The last node to be created is connected to the output terminal by a wire. This exception prevents the construction of circuit branches with unconnected ends.

The role of the GA in the synthesis of a circuit is to govern the evolution of both number of byte codes in the list and the specific bytes in each byte code. The GA operates on a population of lists of byte codes, introducing the byte equivalent of mutations. For each member of the population, the unfolding process is carried out, and the electrical performance of the circuit thus synthesized is simulated numerically by the SPICE circuit simulation computer program. The fitness of that member of the population is quantified by a measure of the difference between the desired circuit output and the actual output according to the simulation. For the sake of speed, the GA is implemented in a master/slave parallel-processing scheme in which a controlling computer generates the members of the population and assigns each member to one of a number of other computers that perform the unfolding process, the simulation, and the evaluation of fitness.

At its present state of development, the method excludes some circuit topologies. Nevertheless, it does enable automated synthesis of many practical circuits that have been designed in the traditional way. For example, one practical circuit synthesized by this method is a low-pass filter for an electronic stetho-

scope (see Figure 2). Further development of the method can be expected to remove some of the topological restrictions. The incorporation of three-terminal devices (e.g., transistors) has produced amplifier circuits recently.

This work was done by Jason D. Lohn and Silvano P. Colombaro of Ames

Research Center. Further information is contained in a TSP [see page 1].

Inquiries concerning rights for the commercial use of this invention should be addressed to the Patent Counsel, Ames Research Center, (650) 604-5104. Refer to ARC-14302.

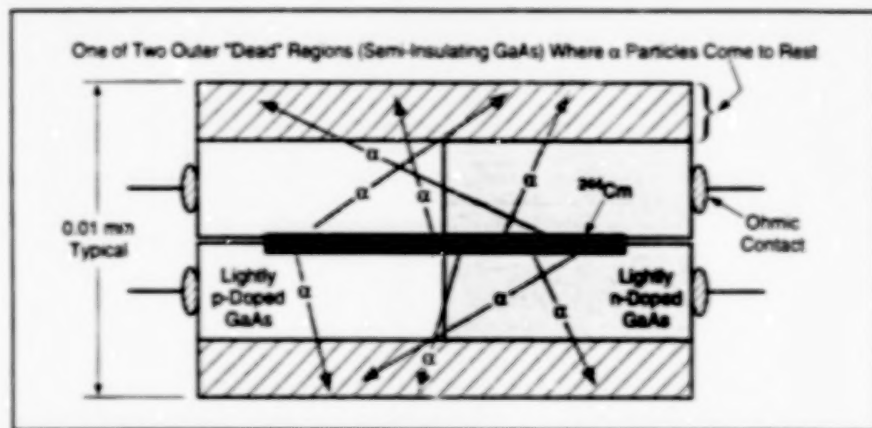
Generating Electric Power From Alpha-Particle Sources

Long-lived, low-power cells could operate for years at extreme temperatures.

NASA's Jet Propulsion Laboratory,
Pasadena, California

Small electric power cells based on the direct conversion of kinetic energy of alpha particles into electricity have been proposed. These cells are expected to function continuously over long times and at temperatures from -250 to 600 °C. They would be made from semiconductors that are stable at high temperatures (most likely GaAs or SiC). The α -particle sources in these cells will likely be made from curium-244, the radioactivity of which is characterized by a half-life of about 18 years and consists nearly entirely of α particles. The proposed cells could be useful as power sources for low-power electronic circuits that are required to operate for long times without recharging or external wire power connections, and without relying on sunlight. Potential outer-space and terrestrial applications could include electronic circuits for spacecraft on long interplanetary or deep-space missions, hearing aids, and surgically implanted medical electronic devices.

Earlier attempts at utilizing α particles to generate electricity have resulted in limited success because of poor planning and lack of proper device designs. Therefore, the planned development of the proposed cells will include studies of factors that affect power-generation efficiency and of the ability of the cells to survive lattice damage induced by impinging α particles. Computer simulations of the effects of different levels of doping of the semiconductors will be performed in an effort to find optimum device designs, and innovative



A Typical Power Cell according to the proposal would have this basic configuration. Tentative parameters for a representative cell capable of generating 0.2 mW of power include dimensions of 1 by 0.2 by 0.01 mm, and ^{244}Cm -source mass of 1 mg.

and device engineering is planned to minimize lattice damage from α particles to maximize device lifetimes and reliabilities.

A basic power cell according to the proposal would include a thin-film α -particle source sandwiched between two p/n diodes (see figure). One key aspect of design that would clearly distinguish a cell of this type from, say, a photovoltaic cell would be choice of diode dimensions so that α particles of the given initial kinetic energy (≈ 5.9 MeV for a ^{244}Cm source) do not stop in the active device volume. The reason for this choice is that α particles cause severe lattice damage in the vicinities of their stopping locations because they lose large fractions of their kinetic energy just before stopping.

Therefore, in the proposed design, outer regions of "dead" semiconductor material would be provided and the dimensions of the p, n, and outer regions would be chosen so that the α particles would come to rest in the outer regions. Although some lattice damage is still expected to occur in the active regions, it has been observed in recent experiments that such damage is continuously annealed during ionization processes in semiconductors.

This work was done by Jagdishbhai Patel of Caltech for NASA's Jet Propulsion Laboratory. Further information is contained in a TSP [see page 1].
NPO-20654

High-Performance Photodetector Circuit for Doppler Lidar

High gain, high bandwidth, and low noise are obtained by careful design.

NASA's Jet Propulsion Laboratory,
Pasadena, California

A photodetector circuit has been built for use in the receiver portion of a continuous-wave infrared Doppler lidar system for atmospheric research. As in nearly all Doppler lidar systems, the

detection of the return signal in this system involves heterodyning, in a photodetector, with a signal at the same frequency as that of the transmitted laser beam. Thus, the Doppler frequencies

manifest themselves as beat frequencies (typically of the order of 40 MHz in this system) that appear in the photodetector output. The reason for developing the present photodetector circuit instead of

using one of the many commercially available photodetector circuits is that a unique combination of high gain, high bandwidth, and low noise is needed for detection of the faint (power as low as 10^{-15} W) return signal in this system.

The present photodetector circuit includes a photodiode, a load resistor, and amplifier circuitry. Ordinarily, a photodiode would be connected to a 50- Ω load resistor because radio-frequency amplifiers capable of handling the Doppler-frequency components of the photodiode output are typically designed for an input impedance of 50 Ω . The load resistance establishes a noise floor in that Johnson noise (expressed as current noise because the photocurrent from the diode is what is to be measured) is inversely proportional to resistance. Thus, if one could use a greater load resistance with the photodiode, then one could lower the noise floor. Accordingly, in this circuit, the photodiode is connected to a 500- Ω load resistance.

The amplifier circuitry comprises an electrically switchable array of commer-

cial two-channel, low-noise video multiplexer/amplifiers that are compatible with the increased input impedance of 500 Ω . Each multiplexer/amplifier has a nominal gain of 4 and a bandwidth > 100 MHz. Through a 4-bit control word, the number of amplifier stages can be set at 3, 4, 5, or 6. In addition, a factor-of-two attenuator can be interposed between the next-to-last and last amplifier stage. The net result is that the gain can be electrically switched (or, equivalently, digitally programmed) to values from 8 to 1,024 in eight factor-of-two (± 6 -dB) steps to accommodate various input signal levels.

To obtain a required overall bandwidth of 60 MHz and to minimize coupling of noise, the circuit must be designed to minimize parasitic capacitance. This is especially true for the node that includes the anode of the photodiode, one end of the load resistor, and the input terminal of the first amplifier stage; every additional picofarad of capacitive loading of this node reduces the overall amplifier bandwidth by about 20 percent. In the design of the circuit, the parasitic capacitance is minimized

through optimal choice of the geometry of the circuit, including the placement of components.

Two other outstanding features of the circuit are the following:

- An operational-amplifier-based servo loop actively regulates the photodiode bias current to prevent saturation of the first amplifier stage in the presence of bright background light, and
- An inverter chip is placed in the digital gain-control pathway to prevent entry of noise on the gain-control lines.

At the time of reporting the information for this article, the circuit had been constructed but not yet tested. The combination of high load resistance, low capacitance, and low-noise amplifiers with high frequency response is expected to yield (1) a noise floor 8 dB below the Johnson noise in a 50- Ω resistor and (2) gain bandwidth as much as 400 GHz.

This work was done by Greg Cardell of Caltech for **NASA's Jet Propulsion Laboratory**. Further information is contained in a TSP [see page 1].
NPO-20558



Electronic Systems

Hardware, Techniques, and Processes

- 13 The KSC Simulation System
- 14 Improved System for Locating Lightning Strikes Within Meters
- 15 Second-Generation Spaceborne Rainfall-Profiling Radar System
- 16 Real-Time Optoelectronic Particle-Fallout Monitors
- 16 Small Lidar Altimeter Would Operate at Low Light Levels

The KSC Simulation System

Better simulations are performed by use of improved hardware and software.

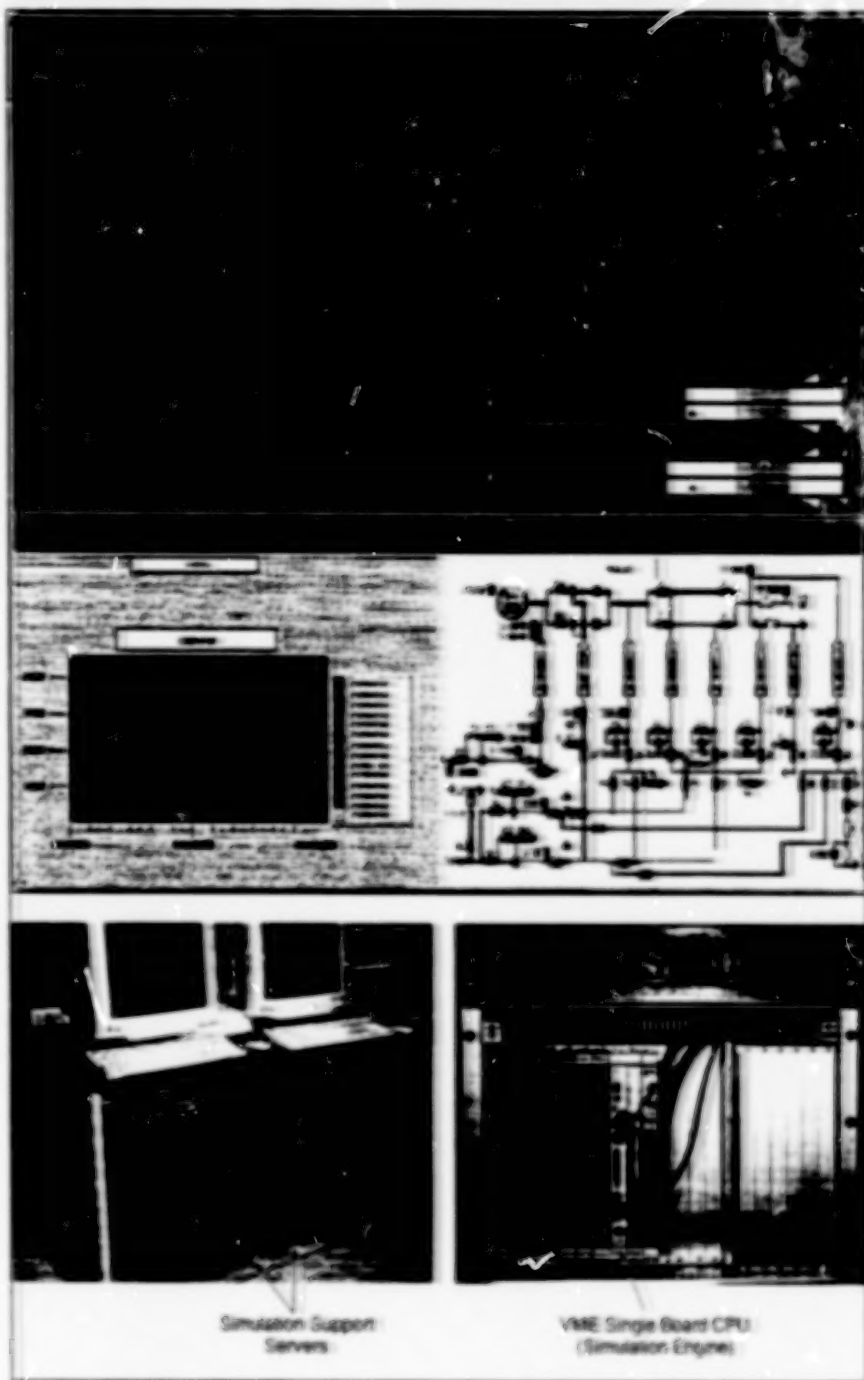
John F. Kennedy Space Center,
Florida

The Kennedy Space Center (KSC) Simulation System is a computing system capable of large-scale mathematical modeling for real-time simulation of the behavior of a complex system that could include many different interacting machines, instruments, and/or computers along with human operators. Developed for simulating space-shuttle launches to ensuring the readiness of launching systems and personnel, the KSC Simulation System could also be adapted to other (including commercial) applications in which there are requirements for real-time simulation of systems represented by large mathematical models.

Previously, launch simulations at KSC were performed on a system called the "Shuttle Ground Operations Simulator" (SGOS), that consisted mainly of a large mainframe computer running a mixture of Fortran and assembly code. The SGOS hardware and software were nonportable, very difficult to debug, and expensive to maintain. Because of increases in the cost of maintenance and aging of the mainframe computer, it became necessary to design the present KSC Simulation System as a more cost-effective, more reliable, and more maintainable replacement for the SGOS.

The SGOS was used in conjunction with a system, called the "Video Simulation Interface" (VSI), that enables communication and flow of data between the KSC Firing Room launch software and the SGOS. In operation, the SGOS appears to engineers in the Firing Room as though they were controlling and monitoring the real space shuttle and its ground support systems. The use of the SGOS thus made it possible to debug the Firing Room software in safety; that is, without jeopardizing the real space shuttle and other hardware. In addition, the SGOS made it possible to train Firing Room personnel by enabling them to experience simulated launch countdowns, into which random failure scenarios were introduced by trainers. The SGOS also made it possible to observe the effects of new hardware and software on the overall launch system before use in a real launch.

In developing the KSC Simulation System, the basic functionality of the SGOS as described above was preserved, as well as its name. The development was accomplished without any effect



The new KSC Simulation System utilizes the latest technology and is designed to provide the capability to support future launch vehicles.

on the rest of the simulation infrastructure at KSC, from the perspective of human users and pre-existing simulation equipment with which the System is required to interact. The System functions identically to the earlier SGOS, except that it is an order of magnitude faster and supports higher-fidelity, larger models. Models in the KSC

Simulation System can have up to 200,000 variables and >16,000 model segments, each segment representing a specific piece of hardware or software. The System can support >1,000 control-procedure programs, which simulate the model. The System can execute a simulation model in real time in steps as small as

5 ms. It supports a sophisticated graphic display path and tracing mechanism. The system includes an extremely easy-to-use human/machine interface for all phases of development and execution of the models and of control procedure programs that stimulate the models.

The central processing unit of the KSC Simulation System computer is a VersaModule Eurocard (VME) single-board computer that communicates with other VME boards inside the VSI. Whereas the SGOS ran on the main-frame computer that occupied more

than half of the second floor of the KSC launch-control-center building, the computer hardware of the present system occupies about the same floor space as that of an ordinary desk (see figure). The computer now runs an entire space-shuttle-launch-countdown simulation of >100MB in real time. The System takes advantage of a broad spectrum of current supporting hardware and software, including 100-Mb/s Ethernet, VMEbus, X-Window/Motif interfaces, and the Unix operating system. The software for the Simulation System itself has been writ-

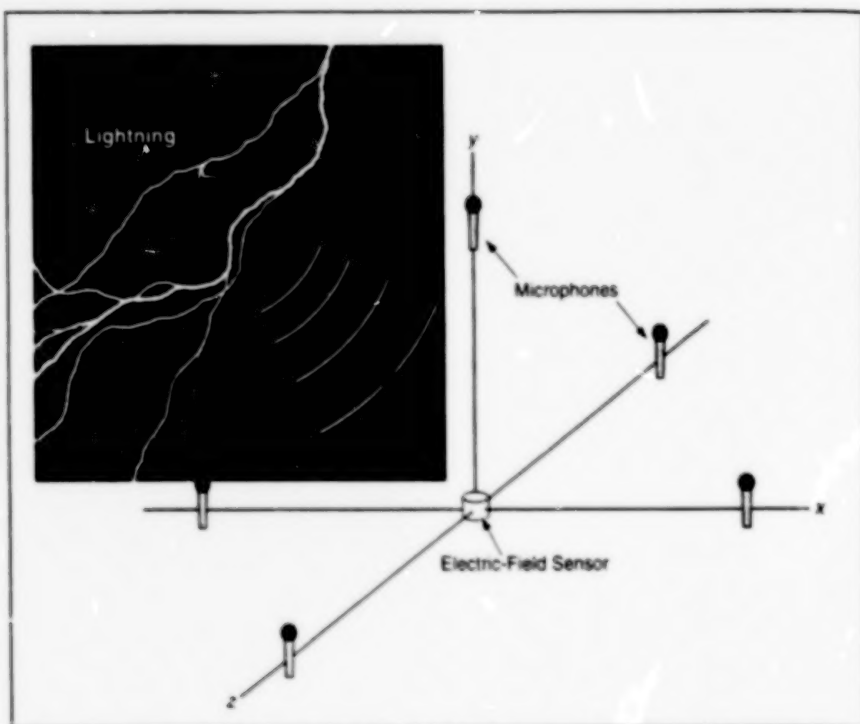
ten in the C, Flex, and Bison (Lex and Yacc) languages, thereby making the software portable to other systems.

This work was done by Scott Estes, Juan M. Busto, Mike Dick, Kevin J. Grant, Jimmy H. Celsor, Charles T. Lostrascio, Nathan G. Taylor, and Carlos M. Alvarado of **Kennedy Space Center** and P. Keith Sullivan, Thomas D. Miller, Caroline A. Achee, John Coulter, and Lauren N. Graves of **United Space Alliance**. Further information is contained in a TSP [see page 1].
KSC-12121

Improved System for Locating Lightning Strikes Within Meters

Distances and bearings are determined from propagation times for electric fields and thunder.

*John F. Kennedy Space Center,
Florida*



An **Electric-Field Sensor** and **Five Microphones** are positioned on the axes of a Cartesian coordinate system, with the microphones at a radius of 1 or 2 m from the origin. The distance and direction of the lightning is determined by the differences among the times of arrival of the electric-field and acoustic signals.

A system for determining the locations of nearby lightning strikes from electric-field and acoustic measurements has been developed. This system evolved from the system described in "System Locates Lightning Strikes to Within Meters" (KSC-11992) NASA Tech Briefs, Vol. 24, No. 7 (July 2000), page 38. The basic concept of both the present and the previous system is an extension of the concept of estimating the distance of a lightning strike from the difference between the times of arrival of the visible flash and the audible thunder.

Like the previous system, the present system locates lightning strikes to within errors of the order of a meter. However, the present system is more compact and more readily deployable, as explained below.

The previous system included a network of at least three receiving stations at locations up to about 0.8 km apart from each other and from the general area wherein lightning strikes of interest could occur. Each receiving station was equipped with an antenna for measuring the electric field generated by a lightning strike and a

microphone for measuring the associated acoustic field (thunder). For each strike, the system measured the difference between the times of arrival of the electric-field and thunder pulses at each station, computed the distance of the strike from the time difference and the speed of sound (about 330 m/s), then used the distances from all three (or more) receiving stations to determine the location of the strike.

The main disadvantage of the previous system was the need to set up multiple receiving stations and to lay power and data cables to connect the receiving stations to a central data-collecting station. In contrast, the present system includes only one receiving station and can thus be set up more quickly and easily.

The single receiving station in the present system (see figure) includes an electric-field sensor at the center of a horizontal circle of 1- or 2-m radius, four microphones placed on the circle at 90° intervals, and a fifth microphone 1 or 2 m above the center. A nearby lightning strike causes the electric-field sensor to put out a pulse that is used to start a timer and to trigger the digitization and recording of microphone outputs as functions of time.

The differences between times of arrival of thunder at the five microphones range up to a few milliseconds. These differences are determined, within <10 μ s, from real-time digital cross-correlations among the microphone outputs. The direction from which the thunder came (and thus the direction to the lightning strike) is computed by finding the set of direction cosines of the sound-propagation vector that yields the least-squares best fit to the time-of-arrival differences, given the known microphone position vectors and the known

speed of sound. For the purpose of computing the direction, it is assumed that the distance to the lightning strike is much greater than the microphone baseline. This distance is readily computed from the time between the measured electric-field pulse and the time of arrival of thunder at one of the microphones.

The main challenge observed during field tests of the system lay in determining the starting times of thunder signals. A thunderclap of interest from a nearby lightning strike can be accompanied by (1) thunder from an earlier and more distant lightning strike, and/or (2) popping sounds generated by streamers that occur alongside the main lightning current path and carry a small fraction of the total current. Because higher-frequency sounds are attenuated over distance more than lower-frequency sounds are, one can discrimi-

nate against thunder of distant origin by high-pass filtering (the filter cutoff frequency used in practice is 100 Hz).

Both the thunderclap of interest and the popping sounds consist primarily of frequencies up to several kilohertz, but a typical thunderclap lasts >100 ms, while the popping sounds are of much shorter duration. Thus, one can distinguish between the sound from the main current path and the sounds from the streamers by discarding short, high-frequency signals. The starting time of the thunder signal is thus identified as the starting time of a high-frequency signal that lasts at least 100 ms. The portion of the history of each microphone output chosen for use in computing the cross-correlations is the portion starting 50 ms before and ending 50 ms after the starting time identified in this manner.

This work was done by Curtis M. Ihlefeld

of Kennedy Space Center and Pedro J. Medelius, Howard James Simpson, and Stan Starr of Dynacs Engineering Co., Inc. Further information is contained in a TSP [see page 1].

In accordance with Public Law 96-517, the contractor has elected to retain title to this invention. Inquiries concerning rights for its commercial use should be addressed to

Michael Guzman

New Technology Administrator

Dynacs Engineering Co., Inc.

P.O. Box 21087

Kennedy Space Center, FL 32815

(321) 867-3322

Fax: (321) 867-7534

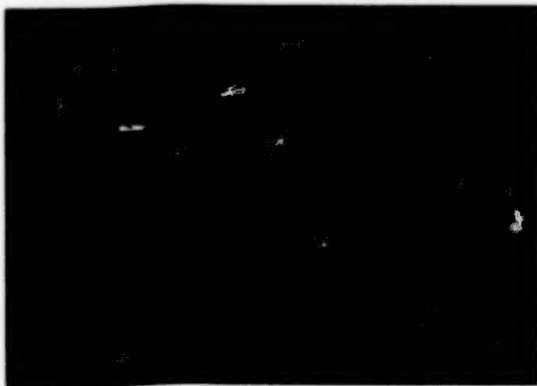
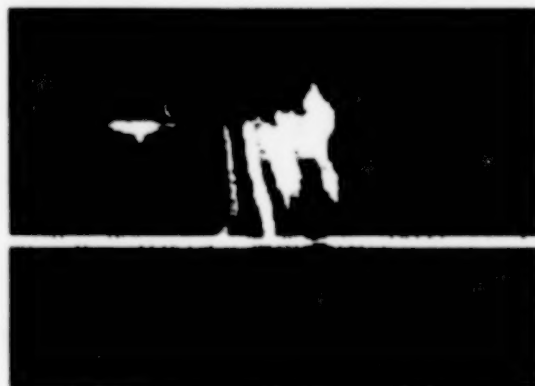
E-mail: GuzmanMA@ksc.nasa.gov

Refer to KSC-12035, volume and number of this NASA Tech Briefs issue, and the page number.

Second-Generation Spaceborne Rainfall-Profiling Radar System

Improvements would include wider coverage and increased resolution.

NASA's Jet Propulsion Laboratory,
Pasadena, California



The Same Scene Can Look Different in radar returns at different polarizations, as shown in this example of like- and cross-polarization reflectivity profiles generated by NASA's Airborne Rain Mapping Radar. Corresponding differences in radar returns from regions of precipitation yield information on the shapes of precipitation particles.

"PR-2" denotes a proposed spaceborne radar system for measuring three-dimensional rainfall profiles and rainfall velocities. The PR-2 system would incorporate a number of improvements over the precipitation radar (PR) system now operating aboard the satellite of the Tropical Rainfall Measuring Mission (a joint project of the United States and Japan).

The improvements and their rationale are the following:

- **Dual-Frequency Radar:** The PR system operates at a carrier frequency of 13.8-

GHz, for which the system is less sensitive to back-scattering from smaller raindrops. The PR-2 system would operate at frequencies of 13.6 and 35 GHz, so that it would be sensitive over a greater range of drop sizes and rainfall rates. The 35-GHz channel would significantly increase the sensitivity of the system to light rain and drizzle. The use of the two frequencies would also reduce errors caused by uncertainties in drop-size distributions.

- **Larger Antenna to Increase Horizontal**

Resolution: At an altitude of 400 km, the horizontal resolution of the PR is about 4 km — about twice the horizontal dimensions of typical convective cells in the tropics and subtropics. Thus, there is a need for at least double the horizontal resolution of the PR. In the PR-2 system, a horizontal resolution of about 2 km would be obtained by use of a larger antenna. Avoiding the increase in weight that would be occasioned by a larger rigid antenna, the antenna in the PR-2 system would be of an advanced, light-

weight, deployable type.

- **Doppler Measurements:** By use of Doppler-signal-processing techniques, it should be possible to measure vertical velocities of raindrops to within ≈ 1 m/s.
- **Like-Polarized and Cross-Polarized Measurements:** The PR-2 system would be made capable of measuring like- and cross-polarized radar back scatter (see figure) in order to exploit polarimetric techniques for distinguishing among precipitation particles of different types (e.g., raindrops versus graupel).
- **Chirp and Pulse Compression:** Because raindrops scatter radar signals weakly in comparison with land and ocean surfaces, rain mapping demands relatively high peak radar-transmitter power; equivalently, it is difficult to obtain enough rain-detection sensitivity at a given

power level. In the PR-2 system, increased sensitivity (without need for increased power) would be afforded by use of relatively long-duration pulses that would be chirped (frequency-modulated) so that most of radar echoes would be redirected into range bins of the target of interest (rain).

- **Wider Ground Swath and Adaptive Scanning:** The PR-2 system would cover a ground swath about 600 km wide (it is about 220 km wide in the PR system). In the absence of other provisions, observation over a wider swath would entail a significant reduction in the time available to dwell on any spots of interest. However, scanning over the whole swath would be wasteful because rainfall usually occurs over a small fraction of the observed area.

Therefore, the PR-2 system would be designed to implement an adaptive-scanning technique, in which it would largely ignore regions of no rainfall and thus have more time to dwell on regions that contain rainfall.

- **Flexible Design:** The PR-2 system would be designed so that its timing and pulse parameters could be adjusted for use on different spacecraft moving in different orbits.

This work was done by Eastwood Im, Stephen Durden, and Ziad Haddad of Caltech and by Eric Smith of FSU for NASA's Jet Propulsion Laboratory. Further information is contained in a TSP [see page 1].
NPO-20761

Real-Time Optoelectronic Particle-Fallout Monitors

These instruments would extract quantitative data from images of particles.

Optoelectronic instruments for real-time, *in situ* monitoring of particle fallout are undergoing development. Settings in which these instruments could prove useful include clean rooms for assembly of optical and electronic equipment, food-packaging facilities, and other industrial facilities in which one seeks to prevent contamination of products by airborne dust and fibers.

Heretofore, it has been common practice in particle-fallout monitoring to place initially clean witness plates in the affected work areas, expose them for suitable amounts of time, then take them to laboratories for analysis. Among the disadvantages of this practice are that it does not provide data in real time, and handling of the witness plates can alter the particle samples prior to analysis. Some optoelectronic instruments for real-time and post-exposure analysis of particle fallout have

been developed previously, but none has offered the combination of features afforded by the present developmental instruments; namely, real-time operation, imaging of individual particles, and quantitative information on numbers and dimensions of particles.

A typical instrument of this type includes a witness plate mounted above a charge-coupled-device (CCD) or other video camera. The witness plate is illuminated to provide uniform omnidirectional lighting. The camera optics are adjusted to focus on the exposed surface of the witness plate, so that particles that have fallen onto the surface are imaged by the camera. The video output is digitized.

The resulting digital image data is processed by image-analysis software that detects particle edges, maps the particles, counts the particles, and determines principal dimensions and aspect ratios of the

John F. Kennedy Space Center,
Florida

particles. The software uses aspect ratios to indicate distinctions between fibers (typical aspect ratios $>10:1$) and other particles. Instruments of this type can detect and measure particles with dimensions down to somewhat less than $10\ \mu\text{m}$.

This work was done by Paul A. Mogan of Kennedy Space Center and Christian J. Schwindt and Timothy R. Hodge of I-NET. For further information please contact:

The Aerospace Engineering Group of
IDEA, LLC
Harvey E. Rice, Jr., President
12240 Indian Creek Court
Suite 105
Beltsville, MD 20705-1242
Tel. No: (301) 419-2922
Fax: (301) 210-4122
E-mail: harvrice@clark.net
KSC-11809

Small Lidar Altimeter Would Operate at Low Light Levels

Relatively high resolution would be achieved without resorting to high power.

A lidar apparatus called a microaltimeter has been proposed for use aboard a spacecraft in orbit around the Earth for mapping land and sea surfaces, including such features of special interest as ice, tree canopies, and flood plains. The microaltimeter is short for "microlaser altimeter" and is so named because it uses a very

compact, low-energy, subnanosecond pulse, solid-state microlaser as its source and relatively small (typically 10 to 20 cm in diameter) telescopes, resulting in a factor of 100 reduction in telescope weight and volume, as compared to conventional spaceborne laser altimeters. Operating at thousands of pulses per second, the sur-

face sampling rate is approximately 100 times higher than that of prior spaceborne laser altimeters having the same transmitter power-aperture product.

Many of the design concepts to be embodied in the microaltimeter, and the components to be used to implement the concepts, were derived from an eye-safe

Goddard Space Flight Center,
Greenbelt, Maryland

satellite laser ranging station called SLR2000. The laser in the microaltimeter would operate at a wavelength of 532 nm, a pulse energy of the order of a millijoule or less, and a pulse-repetition frequency of the order of several kilohertz. The receiver in the microaltimeter would operate in a photon-counting mode, with a mean signal level on the order of one photoelectron per laser pulse. With an ability to measure the times of flight of individual photons and to determine their origin within the receiver field of view through the use of pixellated or

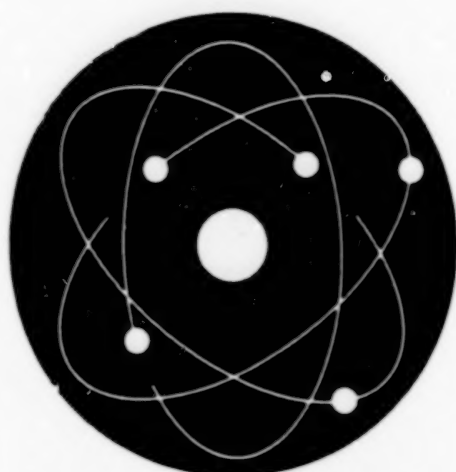
imaging detectors, the receiver can provide ranging unambiguous registration of range (and thus height) data with surface locations.

The theoretically predicted performance of the microaltimeter has been tentatively verified in simulations of the operation of the microaltimeter from Earth orbit, performed by use of software developed previously for simulating the operation of the Mars Orbiter Laser Altimeter (MOLA) and the Geoscience Laser Altimeter System (GLAS). In addition to its potential utility for

Earth science, the microaltimeter could likely be used to rapidly generate nearly contiguous maps of other planets, moons, comets, and asteroids.

*This work was done by John Degnan of **Goddard Space Flight Center**.*

This invention is owned by NASA, and a patent application has been filed. Inquiries concerning nonexclusive or exclusive license for its commercial development should be addressed to the Patent Counsel, Goddard Space Flight Center [see page 1]. Refer to GSC-14098.



Physical Sciences

Hardware, Techniques, and Processes

- 21 Improved Methods of Testing Cryogenic Insulation Materials
- 22 Improved Infrared Imaging of Bulk Defects in CdZnTe Wafers
- 23 Image Generators With Compact Optics
- 24 Electrohydrodynamic Pumping Enhances Operation of Heat Pipe
- 25 Hand-Held Instrument for Imaging Hydrogen Fires
- 26 Improvements in Computed-Tomography Imaging Spectrometry

Improved Methods of Testing Cryogenic Insulation Materials

Specimens are easy to fabricate, and thermal performance measurements are repeatable.

John F. Kennedy Space Center,
Florida

Two improved methods have been developed for testing continuously rolled blankets and blanketlike thermal-insulation materials typically used in cryogenic vacuum systems. Both methods, and their corresponding apparatuses, are based on the cryogen boiloff calorimeter method according to which the amount of heat that passes through an insulation specimen to a cryogenic fluid in a vessel is proportional to the rate of boiloff from that vessel. The boiloff rate is then directly related to the insulating performance of the specimen. The main challenges in the execution of this technique are to (1) eliminate (or minimize) heat leak from the ends by use of thermal guards and (2) obtain stability of the cryogen inside the measurement vessel coincident with stability of the boundary conditions in the vacuum space.

The main problem in testing high-performance materials such as multilayer insulation is the extreme care that must be exercised in their fabrication and installation. Inconsistency in wrapping techniques is the dominant source of error and poses a basic problem in the comparison of such materials. Improper treatment of the ends or seams can render a measurement several times worse than predicted. Localized compression effects, sensor installation, and outgassing are further complications. To eliminate the seam and minimize these other problems, two new methods of fabricating and testing cryogenic insulation systems have been developed.

The first method includes a cryostat test apparatus (Cryostat-1, see Figure 1), which is a liquid nitrogen boiloff calorimeter system for direct measurement of the apparent thermal conductivity at a fixed vacuum level. The cold mass is a 167-mm-diameter, 900-mm-long, vertical stainless-steel cylindrical vessel subdivided into a 10-liter measurement vessel and 2.5-liter thermal-guard vessels at both ends. Continuously rolled materials are installed around a cylindrical copper sleeve using a 1-m-wide wrapping machine. Sensors are placed between layers of the insulation to obtain temperature-thickness profiles. The sleeve is then simply slid onto the vertical cold mass of the cryostat.

During operation, all three vessels are kept filled with liquid nitrogen at near saturated condition at ambient pressure (temperature ≈ 77.8 K). Vacuum levels may be set at any desired pressure from 10^{-5} torr to 760 torr. The temperatures of the cold



Figure 1. Cryostat-1 for testing thermal-insulation materials is shown with a specimen in place. An extra copper sleeve has been stood alongside for reference.

mass, the sleeve (cold boundary temperature), the insulation outer surface (warm boundary temperature), and the vacuum can (heated by a thermal shroud) are measured. The steady-state measurement of insulation performance is made when all temperatures and the boiloff flow rate are stable. The apparent thermal conductivity value of the insulation is directly determined from the measured boiloff rate, boundary temperature difference, latent heat of vaporization, and geometry of the test specimen. The measurable heat gain rate for Cryostat-1 is from 0.2 to 20 W.

This method offers the following advantages:

(1) enables testing of continuously rolled samples for better accuracy, (2) specimens are representative of most industrial applications, (3) specimens can be easily produced to the desired specifications with an absolute minimum of handling, and (4) specimens can be fabricated off-site.

The second method includes a cryostat test apparatus (Cryostat-2, see Figure 2), which is a liquid nitrogen boiloff calorimeter system for calibrated measurement of the apparent thermal conductivity at a fixed vacuum level. The cold mass is a 132-mm-diameter, 267-mm-long stainless-steel vessel thermally guarded by a 132-mm-

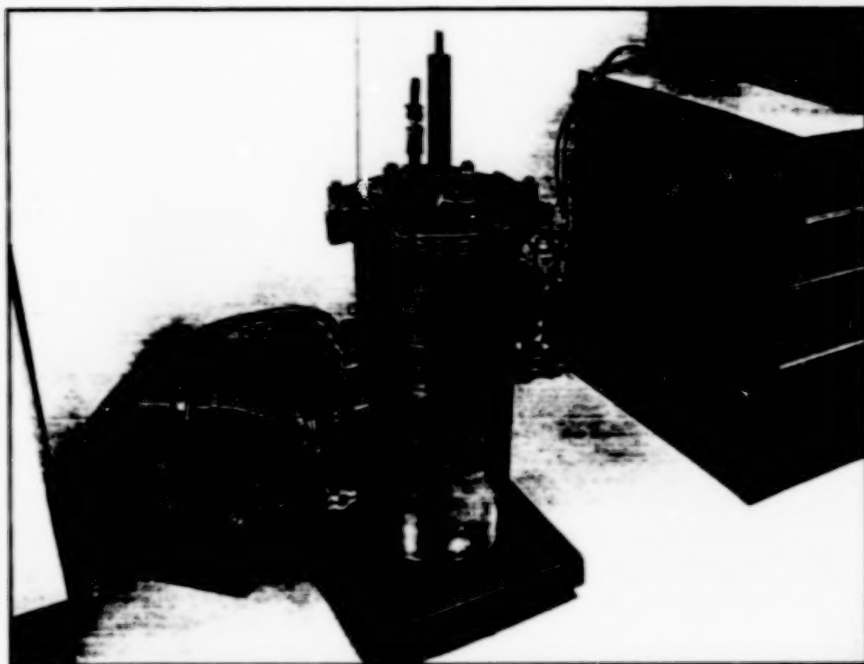


Figure 2. The Overall Test Setup for Cryostat-2 is shown.

diameter, 127-mm-long stack of aerogel composite disks at each end. The system features a fully removable cold mass which quickly and easily mounts onto a 0.5-m-wide wrapping machine for installation of insulation material and sensors.

Cooldown and filling of the system are conveniently accomplished through a single port, using a custom ambient-pressure-regulated liquid nitrogen transfer device. Sensors and measurements are similar to those of Cryostat-1. The measurable heat gain rate for Cryostat-2 is from 0.7 to 40 W. The key benefit of this method is that it allows a high rate of testing many different samples with highly repeatable results between runs.

This work was done by James E. Fesmire, Robert A. Breakfield, Dale J. Ceballos, Philip D. Stroda, and James P. Niehoff, Jr., of **Kennedy Space Center** and Stan D. Augustynowicz of Dynacs Engineering Co. Further information is contained in a TSP [see page 1].
KSC-12107/08

Improved Infrared Imaging of Bulk Defects in CdZnTe Wafers

Images would guide the "mining" of large wafers for fabricating x-ray detectors.

*Goddard Space Flight Center,
Greenbelt, Maryland*

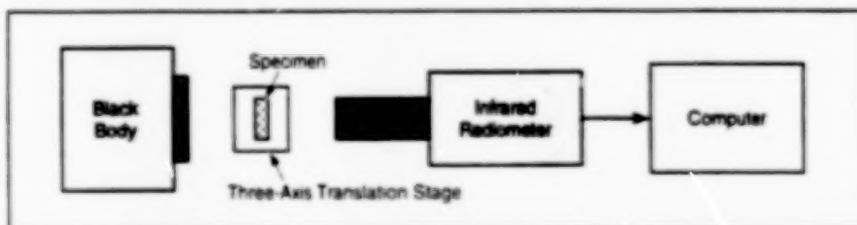


Figure 1. **Black-Body Infrared Radiation** passes through a specimen and is detected by a radiometer to form an image of bulk defects in the specimen.

An improved method of infrared imaging of bulk defects in cadmium zinc telluride (CdZnTe) wafers has been developed. The method is intended primarily to be a means of identifying those portions of large CdZnTe wafers that are suitable to be "mined" for use in fabricating focal-plane arrays of photodetectors for x-ray and γ -ray astronomy. Suitable portions are those that exhibit acceptably high degrees of uniformity of x-ray spectral response. The present method of infrared imaging is useful for identifying the suitable portions because, as described below, there is a correlation between (1) x-ray spectral responses and (2) infrared images of bulk defects that affect those responses.

Prior to the development of the present method, numerous investigators had used infrared-transmission imaging to docu-

ment the distribution of bulk defects in CdZnTe. Incandescent lamps were used as the sources of radiation, and the infrared images were detected by silicon charge-coupled-device cameras operating at wavelengths just beyond the visible range. The present method is also one of infrared transmission imaging, but the wavelength range and the means of implementation are different.

Figure 1 schematically depicts the apparatus used in the present method. The source of radiation is a large-area black body at a temperature of 70 °C. The radiation detector is an infrared radiometer that operates in the wavelength range of 8 to 12 μ m; it includes an HgCdTe photodetector cooled to 77 K by liquid nitrogen. A three-axis translation stage is used to manipulate a

CdZnTe specimen wafer. Various lenses, including a microscope objective, are used to optimize images of defects.

During the development of the present method, experiments were performed to determine whether the infrared images produced by the apparatus described above could be used to identify the desired portions of CdZnTe wafers. In these experiments, CdZnTe specimen wafers of two different sizes (15 by 15 by 2 and 26.9 by 26.9 by 2 mm) were set up as planar photodetectors and exposed to a collimated beam of x rays from a 16-kV microfocus x-ray tube. The collimated beam was either 100, 250, or 500 μ m wide. Each specimen was mounted on a computer-controlled, motorized translation stage and was translated in 100, 250, or 500 μ m increments across the detector plane. At each increment of position, the CdZnTe detector output was processed into an x-ray-spectral response by a simple pulse-height-analysis system.

The bulk defects that can be seen in the infrared images include grain boundaries and twin boundaries decorated with tellurium inclusions, and pipe-like voids. The results of the experiments show that there is a correlation between poor x-ray-spectral response and grain boundaries decorated

with tellurium inclusions (see Figure 2).

It would be natural to ask why the infrared imaging method is preferable to generation of x-ray spectral images of wafers. The answer is simply that it would take a long time to scan a wafer [about 60 hours at 500- μ m resolution for a 5-in. (127-mm)-diameter wafer] and most of that time would be wasted because of large defect densities encountered in practice. Instead, one could use the present infrared-imaging method to screen an entire wafer quickly to identify areas with acceptably low defect densities and dimensions large enough for fabricating photodetector arrays.

This work was done by Bradford Parker, J. Timothy Van Sant, Richard Mullinix, C. M. Stahle, A. M. Parsons, and J. Tueller of Goddard Space Flight Center, Bruno Munoz of Unisys Corp., S. D. Barthelmy of Universities Space Research Associates, and S. J. Snodgrass of Raytheon STX. Further information is contained in a TSP [see page 1].
GSC-14255

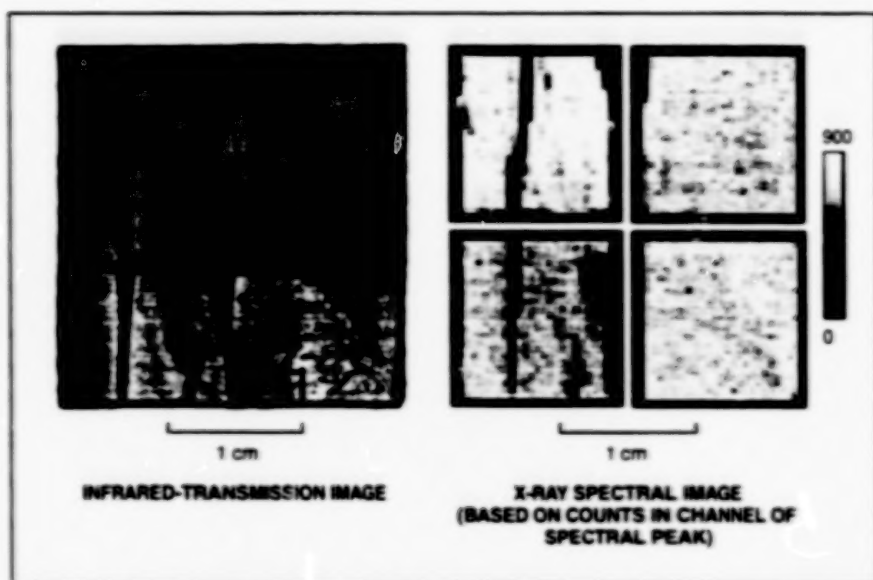


Figure 2. Infrared-Transmission and X-Ray Spectral Images of the same CdZnTe specimen exhibit correlations that can be useful in selecting relatively-defect-free areas for fabrication into focal-plane arrays of x-ray detectors. The x-ray spectral image comprises four subimages because for operation of the CdZnTe specimen as an x-ray detector, it was necessary to subdivide its anode contact into four areas to reduce leakage noise.

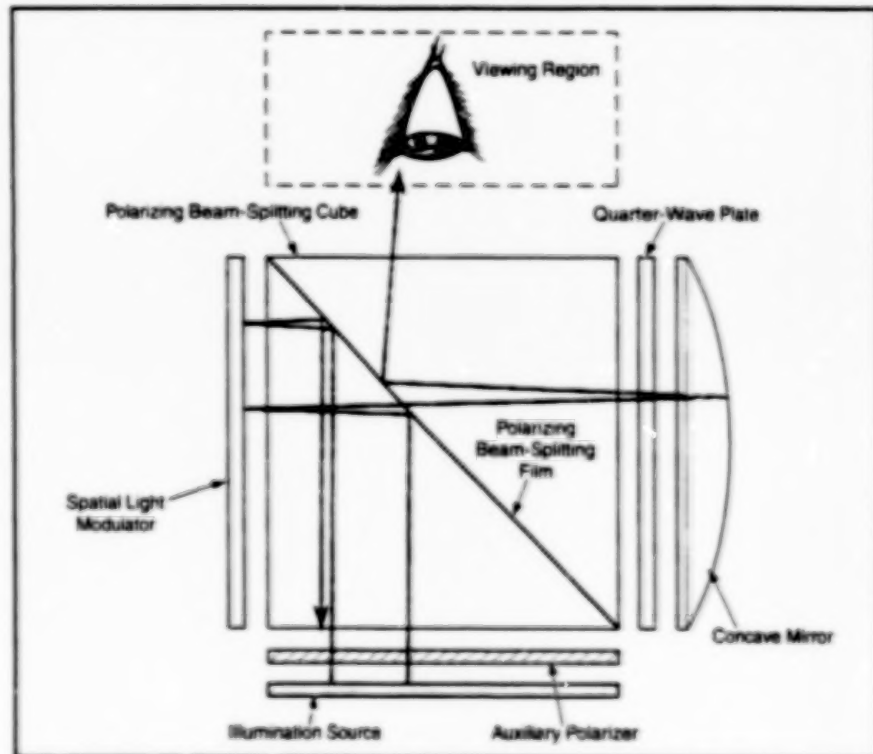
Image Generators With Compact Optics

These devices can be used for head-mounted, helmet-mounted, and eyeglass-mounted displays.

Lyndon B. Johnson Space Center,
Houston, Texas

Compact image generators that contain illumination sources and electronically controlled spatial light modulators have been invented. Compactness is achieved by folding of the optical paths that link the illumination sources, the spatial light modulators, and the viewing regions into which images are projected. The optical configuration of a device of this type ensures that a large proportion of the light from the illumination source is directed into the viewing region; consequently, the device is unusually energy-efficient for a display device and can, therefore, be operated at a relatively low power (possibly even battery power) for a given display brightness. By virtue of their compactness and low power consumption, these image generators are suitable for head-mounted, helmet-mounted, and eyeglass-mounted displays.

These image generators can be designed in a number of alternative optical configurations, of which one is depicted in the figure. The precise nature of the illumination source is not critical; the source can consist, for example, of one or more light-emitting diodes, laser diodes, cold-cathode or field-emitter cathodoluminescent sources, or incandescent or fluorescent lamps together with a switchable color filter. The spatial light modulator is of a reflective (as distinguished from transmis-



Compactness and Efficient Utilization of Light are achieved by a combination of folding the optical path, polarization, and focusing of light from the modulator and the illumination source.

sive) type that effects modulation by either changing or not changing the polarization of light upon reflection, depending on the

electronically controlled ON/OFF status of each pixel. The modulating medium in the spatial light modulator is typically a ferro-

electric liquid crystal layer.

Light from the illumination source is directed through an auxiliary polarizer into a polarizing beam-splitting cube. The auxiliary polarizer passes only light that is s-polarized with respect to incidence on the polarizing beam-splitting film in the cube. The film reflects most of this s-polarized light toward the spatial light modulator. The light reflected from the spatial light modulator contains the desired image in the form of pixel-by-pixel variations in the proportions of s-polarized and p-polarized light.

The modulated light goes back into the cube, where it is analyzed by the polarizing beam-splitting film: The s-polarized (unchanged) portion of the modulated light is reflected back toward the illumination source. The p-polarized image-bearing light passes through the film, then out of the cube, then through a quarter-wave plate, until it strikes a concave mirror. After reflection from the

concave mirror, this light passes back through the quarter-wave plate.

The double pass through the quarter-wave plate converts the polarization from p to s; consequently, upon striking the polarizing beam-splitting film, this image-bearing light is reflected out of the cube toward a viewing region. The curvature (and thus the focal length) of the mirror is chosen, in conjunction with the other dimensions of the optics, so that (1) to ensure efficient utilization of light, a real image of the illumination source is formed within the viewing region and (2) a magnified virtual image of the pattern of modulated light can be viewed by an eye placed within the viewing region, facing toward the cube.

In some applications, it is desirable to provide for adjustment of the gap between the cube and the spatial light modulator and the gap between the cube and the concave mirror, in order to enable focusing of the viewable image. Optionally, once

these adjustments have been completed, the various optical components, including the cube, can be cemented together to produce a rugged assembly that resists misalignment.

This work was done by Mark A. Handschy, Michael R. Meadows, Martin Shenker, and Paul E. Weissman of Displaytech, Inc., for Johnson Space Center. Further information is contained in a TSP [see page 1].

In accordance with Public Law 96-517, the contractor has elected to retain title to this invention. Inquiries concerning rights for its commercial use should be addressed to

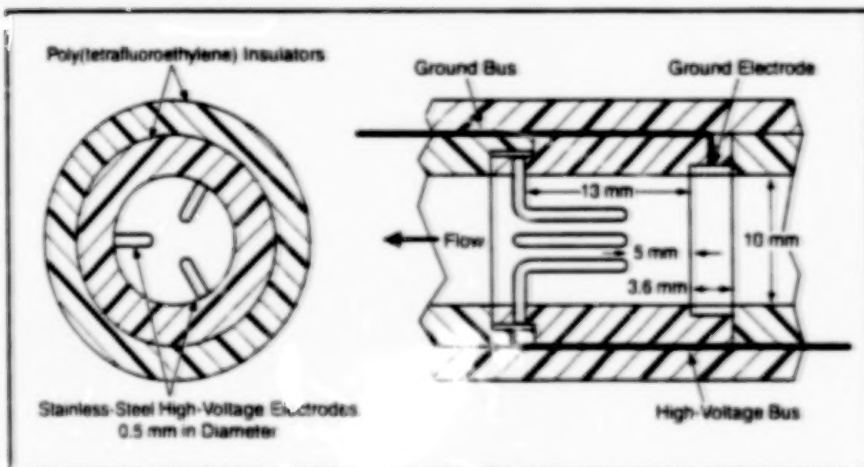
Mark Handschy
Displaytech, Inc.
2602 Clover Basin Drive
Longmont, CO 80503

Refer to MSC-22992, volume and number of this NASA Tech Briefs issue, and the page number.

Electrohydrodynamic Pumping Enhances Operation of Heat Pipe

Heat-transport capacity is increased substantially.

Lyndon B. Johnson Space Center,
Houston, Texas



The EHD Pump installed in the liquid channel of a heat pipe consisted of six electrode stages like this one.

Experiments have shown that electrohydrodynamic pumping can be utilized to increase the heat-transport capacity of a heat pipe. More specifically, electrohydrodynamic pumping can be used to increase the flow of liquid to the evaporator section of the heat pipe; the increased flow helps to prevent dryout of the evaporator during a startup transient or during operation at a high heat-transport rate. Electrohydrodynamic pumping can also accelerate recovery from dryout.

The electrohydrodynamic (EHD) phenomenon is a result of interactions between a dielectric fluid and an applied

electric field. These interactions give rise to the following body forces on the fluid:

- The Coulomb force — the force attributable to the electric field acting on free charges in the fluid;
- The dielectrophoretic force, which is proportional to the square of the magnitude of the electric field and to the gradient of permittivity of the fluid (for example, the sharp gradient at a boundary between the liquid and vapor phases of the fluid); and
- The electrostrictive force, which is proportional to the gradient of the square of the magnitude of the electric field. The

dielectrophoretic and electrostrictive forces are both denoted as polarization forces because they are attributable to the interaction between the electric field and polarization electric charges in the molecules of the fluid.

The particular EHD-pumping design chosen for the experiments utilizes the Coulomb force with no direct injection of electric charges. The EHD pump (see figure) was incorporated into the liquid channel of the adiabatic section (the section between the evaporator and condenser sections) of a monogroove heat pipe in which the working fluid was dichlorotrifluoroethane. In the experiments, the heat-transport capacity was increased by more than 200 percent when a potential of 20 kV was applied to the EHD-pump electrodes. The electric power consumed under this condition was only 0.08 W. In one experiment in which the heat pipe had undergone progressive evaporator dryout for 70 minutes at a heat-transport rate of 400 W, the application of voltage to the EHD pump resulted in essentially instantaneous recovery from dryout.

This work was done by J. Seyed-Yagoobi and J. E. Bryan of Texas A&M University for Johnson Space Center. Further information is contained in a TSP [see page 1].

MSC-22847

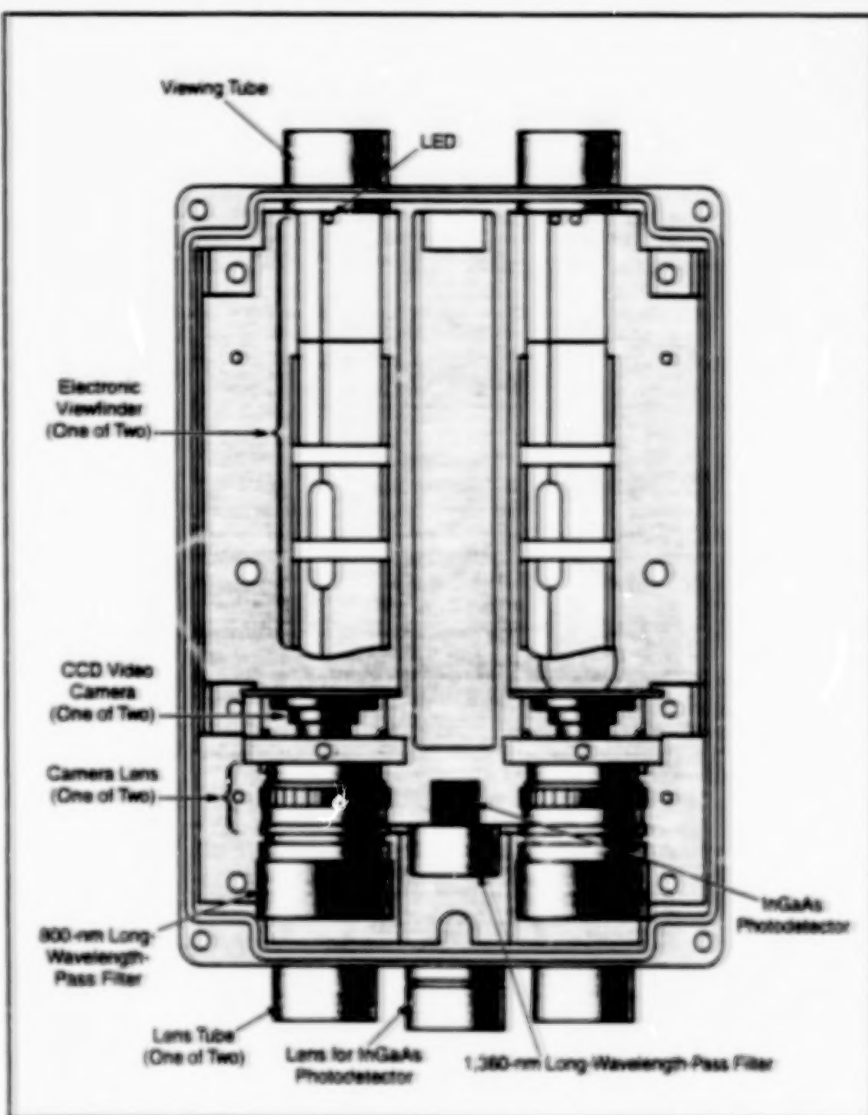
Hand-Held Instrument for Imaging Hydrogen Fires

Hydrogen fires can be seen even in full daylight.

Stennis Space Center,
Mississippi

A hand-held instrument that contains two silicon-based charged-coupled-device (CCD) video cameras (see figure) has been developed for imaging hydrogen fires. This or a similar instrument is needed because the visible light emitted by a hydrogen fire is so dim that the fire cannot be seen by the unaided human eye — at least, not in bright daylight. Like some other CCD-camera-based instruments developed previously for the same purpose, this instrument is designed to operate at infrared wavelengths where hydrogen fires appear bright, relative to solar background light. One CCD camera is called the "cloudy" camera, while the other is called the "sunny" camera, to indicate the different lighting conditions under which the cameras are designed to operate. In front of the "cloudy" camera is a long-wavelength-pass filter with a cutoff wavelength of 800 nm; during overcast, this filter blocks enough background light to make a hydrogen flame appear bright against the background. In front of the "sunny" camera there is a long-wavelength-pass filter with a cutoff wavelength of 1,100 nm; this filter blocks the solar background in the presence of full sunshine, such that a hydrogen flame is brighter than the solar background. The infrared images in the cameras are converted electronically and displayed to the instrument operator as visible images on miniature cathode-ray tubes in electronic viewfinders. A switch enables the operator to select the camera depending on the current light conditions. Optionally, both cameras and their viewfinders can be used simultaneously for binocular viewing.

The instrument includes a nonimaging, InGaAs-based photodetector that has a field of view 40° wide. This photodetector is preceded by a band-pass filter with a nominal pass wavelength of 1,360 nm, which is the wavelength of a peak in the emission spectrum of a hydrogen flame. This photodetector provides additional spectral discrimination of a hydrogen flame; it can also be used to trigger an audible alarm and a visible flash by light-emitting diodes (LEDs) inside the viewfinders, thereby helping to



The Major Components of the Hydrogen-Fire Imager can be seen in this top view of the instrument with its cover removed.

prevent the operator from overlooking a small hydrogen flame.

This instrument can be used to view a hydrogen flame only 8 in. (20 cm) long from a distance of 50 ft (15 m) in full sunlight. It can also be used to image alcohol fires, typical hydrocarbon fires, and embers, which emit in the same spectral regions as do hydrogen fires. Because a hydrogen fire, an alcohol fire, a hydrocarbon fire, or an ember can be seen readily only through the instrument, the operator can readily distinguish between these phenomena and a bright artificial

light or a solar reflection, which can be seen without the instrument.

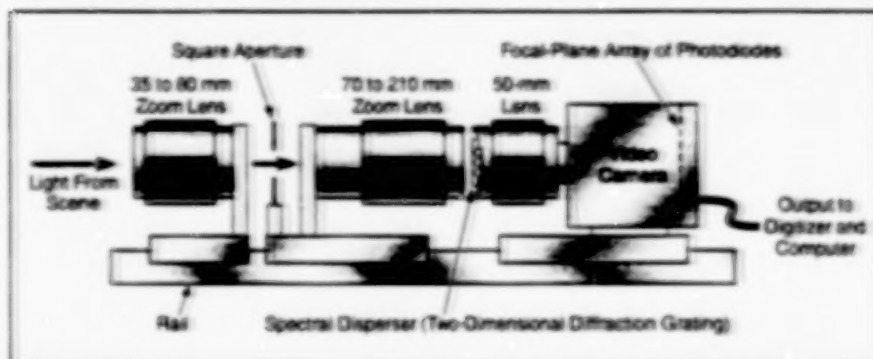
This work was done by Heidi L. Barnes of Stennis Space Center and Harvey S. Smith of Lockheed Martin. Further information is contained in a TSP [see page 1].

This invention has been patented by NASA (U.S. Patent No. 5,726,632). Inquiries concerning nonexclusive or exclusive license for its commercial development should be addressed to the Patent Counsel, Stennis Space Center [see page 1]. Refer to SSC-00040.

Improvements in Computed-Tomography Imaging Spectrometry

CGHs are used for dispersion, and a modified calibration procedure saves time.

NASA's Jet Propulsion Laboratory,
Pasadena, California



This is an **Experimental CTIS**. The heart of this instrument is the two-dimensional diffraction grating, which spectrally disperses an image of the scene in two spatial dimensions. Superior two-dimensional gratings with tailorable properties can be in the form of PMMA computer-generated holograms fabricated by electron-beam lithography and etching.

Two major improvements, described below, have been made in the construction and operation of a computed-tomography imaging spectrometer (CTIS). These plus future improvements can be expected to enhance the practicality and commercial viability of CTISs, which, in principle, offer unprecedented capabilities for imaging with spatial, spectral, and temporal resolution. For example, the CTIS in its present form could be used in medical and pharmaceutical applications to perform spectral imaging of transient scenes that contain fluorescent dyes. With increases in spectral accuracy and spatial resolution, it could be used for remote sensing.

A CTIS includes a spectral disperser in the form of a two-dimensional diffraction grating positioned between two relay lenses in a video imaging system (see figure). If the disperser were removed, the system would produce ordinary images of the scene in the field of view of the system. In the presence of the grating, the image on the focal plane of the system contains both spectral and spatial information because the multiple diffraction orders of the grating give rise to multiple, spectrally dispersed images of the scene. By use of algorithms adapted from computed tomography, the

image on the focal plane can be processed into an "image cube" — a three-dimensional collection of data on the image intensity as a function of the two spatial dimensions (x and y) in the scene and of wavelength (λ). Thus, both spectrally and spatially resolved information on the scene at a given instant of time can be obtained, without scanning, from a single snapshot; this is what makes the CTIS such a potentially powerful tool for spatially, spectrally, and temporally resolved imaging.

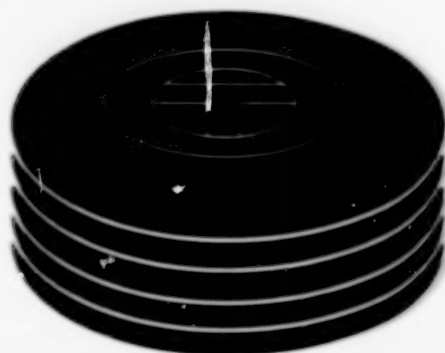
Prior to the improvements reported here, the two-dimensional gratings for CTISs were constructed by stacking and crossing one-dimensional gratings. The disadvantages of this approach are that (1) total throughput efficiency is low, (2) diffraction-order efficiencies cannot be tailored to prevent saturation of focal-plane-array (FPA) photodetectors by weakly dispersed orders, and (3) the pattern of dispersed images does not fill the FPA area efficiently. This leads to the first of the two improvements, which is the use of computer-generated holograms (CGHs) as the two-dimensional dispersers. The CGHs offer high total efficiencies and can be designed to generate arbitrary patterns of diffraction-order efficiencies. The CGHs are made from poly(methyl methacrylate) by analog direct-

write electron-beam lithography followed by development in pure acetone.

To be able to use the computed-tomography algorithms to reconstruct a scene from an image on the focal plane, one must first determine connection weights from positions and wavelengths in the scene to detector pixels. One can determine the connection weights fairly directly by measuring pixel detector outputs while scanning a monochromator-illuminated optical fiber across the scene. Such a complete calibration procedure is hardware-intensive and is time-consuming because the entire scene must be scanned anew for each resolution element in the image cube. This leads to the second improvement, which is a modification of the calibration procedure.

In the modified procedure, one does not scan the entire scene; instead, one uses measurements taken while the single point in the center of the scene is illuminated at each wavelength of interest in the pass band of the CTIS. There are two steps in the modified calibration procedure. In the first step, the pixel outputs are measured at each wavelength. From the measurements, the corresponding system efficiencies (throughput fractions) are calculated for all diffraction orders at all the wavelengths. In the second step, the system efficiencies are used in a ray-tracing computer program that calculates the connection weights from all scene positions to all pixels on the focal plane. The calculation accounts for transmissivities of lenses and other optical elements, plus spectral responsiveness of the photodetectors.

This work was done by Daniel Wilson, Paul D. Maker, and Richard Muller of Caltech and Michael Deslaurier and Eustace Derraniak of the University of Arizona for NASA's Jet Propulsion Laboratory. Further information is contained in a TSP [see page 1].
NPO-20561



Computer Programs

Mechanics

- 29 Program Computes Tone Fan Noise From a Turbofan Engine

Mathematics and Information Sciences

- 29 Software for Generating 100-by-100-km Images From SAR Data
29 Program for Displaying Large, Coregistered Images
29 Sequencing and Job-Control Software for Processing SAR Data
30 Software for Water-Level Testing of Microfabricated Devices
30 Software for Processing RADARSAT ScanSAR Data into Images

Computer Programs

Mechanics

Program Computes Tone Fan Noise From a Turbofan Engine

TFaNS is a computer program that predicts the tone noise that emanates from the fan stage of a turbofan engine. With the help of this program, engineers working to reduce fan tone noise can study the effects of proposed design changes and are thus more likely to be successful in their efforts.

The interaction of the fan wake with the downstream stator vanes is a significant source of fan noise in a modern turbofan engine. Other fan-noise computer codes predict the rotor/stator tone noise and the noise radiated from the inlet and exhaust sections of fan stage separately. Unlike those codes, TFA NS predicts entire noise field, both inside and outside an engine duct. TFA NS takes account of the effects of reflection and transmission by the rotor and stator and by the duct inlet and nozzle; this is done in addition to the conventional mathematical modeling based on a concept of an annular duct and an isolated stator. In other words, TFA NS couples the results from all such computations that, heretofore, were performed separately, in order to generate a complete fan-stage noise prediction.

TFaNS includes the following modules:

- SOURCE3D estimates the strength of the rotor/stator-interaction tone-noise source.
- INLRAD3D and AFTRAD3D predict the propagation of the tone noise from the source, through the fan-duct termination, to the far field.
- CUP3D couples the results from the aforementioned modules to provide a complete fan-stage noise prediction.
- AWAKEN mediates the input, into the SOURCE3D module, of rotor-wake data that have been obtained through either measurement or else simulation by a computational fluid dynamics (CFD) code.

At present, the range of applicability of TFA NS is limited to subsonic fan-tip speeds.

This program was written by David Topol of United Technologies Corp. and Walter Eversman of the University of Missouri-Rolla for **Glenn Research Center**. Further information is contained in a TSP [see page 1].

Inquiries concerning rights for the commercial use of this invention should be addressed to NASA Glenn Research Center, Commercial Technology Office, Attn: Steve Fedor, Mail Stop 4-8, 21000 Brookpark Road, Cleveland, Ohio 44135. Refer to LEW-17063.

Mathematics and Information Sciences

Software for Generating 100-by-100-km Images From SAR Data

SAR Processing System Precision Processor (SPS PP) is one of the computer programs used in the Alaska SAR Facility (ASF) [where "SAR" means "synthetic-aperture radar"] to generate image data products. SPS PP ingests data that have been received from the RADARSAT (a Canadian Earth-observation satellite) and decoded into engineering and SAR signal data files, and processes these data into image data products that typically cover areas of about 100 km by 100 km. SPS PP can handle data from RADARSAT standard right- and left-looking beams, and is being enhanced to handle European Remote Sensing Satellite (ERS) and Japanese Earth Resources Satellite (JERS) data. The output of SPS PP conforms to the standards of the Committee on Earth Observing Satellites (CEOS). The left-looking products feature 16-bit detected pixels in slant-range format; the right-looking products can be in either ground-range detected or slant-range complex format. SPS PP resides on five IBM SP-2 computers with 8 processing nodes each. Each computer can produce a 100-by-100-km image frame in about 25 minutes.

This program was written by Homayan Alaei, Michael Jin, Quyen Nguyen, and Shelby Yang of Caltech for **NASA's Jet Propulsion Laboratory**. Further information is contained in a TSP [see page 1].

This software is available for commercial licensing. Please contact Don Hart of the California Institute of Technology at (818) 393-3425. Refer to NPO-20710.

Program for Displaying Large, Coregistered Images

DataSlate is an easy-to-use Java-language computer program for displaying coregistered raster images representing large sets of data. The program includes a main viewing module that can display image data that have been converted into a special DataSlate format called "SimpleStruct" by use of an Interactive Data Language program called "SimpleGen." The conversion into SimpleStruct optimizes the organization of the data in the sense that it simplifies any computations that must be done subsequently during perusal of the data. DataSlate enables the user to navigate very large sets of scientific data visually. DataSlate presents a slate-like user interface with simple buttons to select sets of data or to zoom in or out. The user can scroll through a set of data by simply dragging a cursor on a screen. DataSlate can also dynamically load plug-in software tools (e.g., for measuring lengths, angles, areas, or geographic coordinates) at run time. DataSlate can also traverse coregistered collections of data and can present a second data channel in a window on the screen to facilitate correlation or comparison of two sets of data (e.g., from two sensors and/or taken at different times).

This program was written by Akos Csikmatory, Michael Martin, Adrian Godoy, David Hecox, Jose Pena, and Jason LaPointe of Caltech for **NASA's Jet Propulsion Laboratory**. Further information is contained in a TSP [see page 1].

This software is available for commercial licensing. Please contact Don Hart of the California Institute of Technology at (818) 393-3425. Refer to NPO-20691.

Sequencing and Job-Control Software for Processing SAR Data

The SAR Processing System Control Processor (SPS CP) computer program performs sequencing and job-control functions within the Alaska SAR Facility (ASF) [where "SAR" means "synthetic-aperture radar"]. SPS CP interacts with the Product-Distribution-and-Management (PDM) system of the ASF to receive processing orders as well as engineering and raw signal data. SPS CP provides a graphical user

interface for operator control and performs job-sequencing functions to orchestrate the Raw Data Scanners (RDS) and SAR processors of the ASF to produce image data products. It is capable of displaying images to support visual data-product-quality checks. It is capable of recovering from errors caused by various abnormal processing events. The interfaces between SPS CP and the raw-data scanners and SAR processors are based on a client-server model with sockets and multithreading. SPS CP is hosted on SGI Origin or Challenge computers; the interfaces with raw data scanners and SAR processors are hosted on SGI Challenge, DEC Alpha, IBM SP-2, and Compaq computers. This program has been supporting ASF operations for over five years and its capabilities have been continuously enhanced to enable both large and small scientific-processing campaigns that have included mapping of the Amazon rain forest, the Antarctic Mapping Mission, and the Arctic Snapshot Mission.

This program was written by Eugene Chu, Daniel Fineman, Pearl Haw, John Ho, Nancy Perry, Cris Sandoval, and Joanne Shimada of Caltech for NASA's Jet Propulsion Laboratory. Further information is contained in a TSP [see page 1].

This software is available for commercial licensing. Please contact Don Hart of the California Institute of Technology at (818) 393-3425. Refer to NPO-20713.

Software for Wafer-Level Testing of Microfabricated Devices

Prober Assistant Measurement System (PAMS) is a computer program that automates the time-consuming process of testing microfabricated devices (integrated

circuits and/or microelectromechanical systems) at the wafer level. PAMS was written specifically for use with the Karl Suss probe station (a commercially available wafer-testing apparatus) and is compatible with associated testing circuitry that conforms to the IEEE 488 general-purpose interface bus (GPIB) standard. Manual wafer testing is tedious and susceptible to error because the process involves controlling the probe station to position the probe leads on each device, configuring the associated testing equipment, and recording the measurement data. In contrast, PAMS automatically positions the probe leads according to a wafer map and automatically performs the measurement and recording steps. Multiple devices on a wafer can be tested simultaneously, or multiple measurements can be made on a single device. Acquired data can be displayed on a screen and/or recorded in a file. At present, PAMS is executed on a computer based on a Pentium II processor with a clock rate of 400 MHz, 128MB of random-access memory, and 6GB of hard-disk storage, and running the Windows NT operating system.

This program was written by Christopher Evans of Caltech for NASA's Jet Propulsion Laboratory. Further information is contained in a TSP [see page 1].

This software is available for commercial licensing. Please contact Don Hart of the California Institute of Technology at (818) 393-3425. Refer to NPO-20850.

Software for Processing RADARSAT ScanSAR Data Into Images

SAR Processing System ScanSAR Processor (SPS SSP) is a computer program that is used in the Alaska SAR Facility

(ASF) to process scanSAR downlink data from the RADARSAT (a Canadian Earth-observation satellite) into a suite of image data products. ["SAR" means "synthetic-aperture radar" and "scanSAR" means "scan-mode SAR."] SPS SSP can process data that have been generated in any of the four RADARSAT scanSAR modes in current use — two wide-swath modes (300 ≤ width ≤ 500 km) called "SWA" and "SWB" and two narrow-swath modes (width ≈ 300 km) called "SNA" and "SNB." The output images are projected in ground range or else geocoded in universal transverse Mercator, polar stereographic, or Lambert coordinates. At present, the only image data products that are calibrated are those of the SWB mode. Typically, an SWB image covers an area of about 500 by 500 km. SPS SSP is executed on an IBM PS-2 computer, which includes (1) a control workstation equipped with 128MB of random-access memory (RAM) and a 4GB hard disk and (2) as many as eight processing nodes, each equipped with 256MB of RAM and a 4GB hard disk. When all eight nodes are used, a typical SWB image frame can be computed in about 35 minutes.

This program was written by Michael Jin, Quyen Nguyen, Jeff Schredder, and Wayne Tung of Caltech for NASA's Jet Propulsion Laboratory. Further information is contained in a TSP [see page 1].

This software is available for commercial licensing. Please contact Don Hart of the California Institute of Technology at (818) 393-3425. Refer to NPO-20712.



Mechanics

Hardware, Techniques, and Processes

33 Asymmetric Dual-Axis Goniometer for Positioning on a Sphere

Asymmetric Dual-Axis Goniometer for Positioning on a Sphere

The bulk, moving mass, and total mass would be reduced substantially as compared to a typical goniometer implementation.

NASA's Jet Propulsion Laboratory,
Pasadena, California

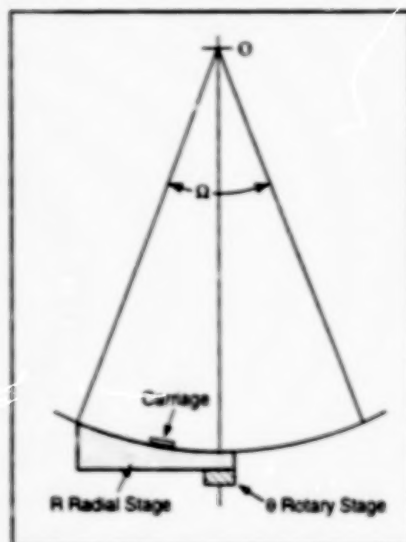


Figure 1. In the R-Theta Goniometer, any position on the spherical surface centered on "O" within the solid angle Ω is accessible to the carriage using R (radial distance from rotation axis) and θ (rotation about axis) motions.

The ability to position an object at various locations corresponding to a portion of a spherical surface has long been accomplished using nested goniometers, in which, as observed from above, the apparent motion is readily described in a Cartesian ("XY") frame. In certain applications, however, a more suitable basis of motion would be described in a polar coordinate ("R-Theta") frame. The implementa-

tion and advantages of such a device is described here.

Figure 1 schematically depicts a proposed device that produces R-Theta based goniometric motion. The curved radial stage, while functionally the same as a conventional single-axis goniometer, is mounted to a rotary stage offset to one end of the radial stage. The resulting device can position an object mounted on the radial stage carriage to any location on the surface of the sphere defined by the curvature and extent of the radial stage.

Figure 2(a) shows the R-Theta device compared to the XY form. As compared to the typical XY nested-goniometer approach, the R-Theta implementation has only 25 percent of the mass, and occupies only 25 percent of the volume. Further, the moving mass of the R-Theta form is 50 percent that of the XY form. Note that these percentages are approximate, and will depend on the exact implementation chosen for the device (for example, material choice and light-weighting techniques, if utilized).

The initial application for which the R-Theta form was designed was for a multiple telescope platform, which required the ability to move four independent telescopes in such a way that all four pointed through a common point in space, while maintaining a fixed distance from

that point. In addition, the scientific requirements of the mission were best served if the four telescopes could also have partially overlapping fields-of-regard on the sky. If implemented in the typical XY form, the necessity of maintaining clearances between all of the moving elements would have forced a larger than desired separation between the telescopes, and could not provide the overlapping fields-of-regard without significantly restricting the total motion of one or more telescopes. By using the R-Theta form instead, a denser packing could be achieved, and by judicious trajectory planning, the significant overlap in the telescope fields-of-regard could be implemented [Figure 2(b)].

As a final note, it is apparent that the carriage on the radial stage experiences a rotation with respect to a global coordinate system as the rotary stage is actuated. If this effect should be undesirable in a given application, a synchronized derotation stage could be added on top of the radial stage carriage; such a stage could also be used to provide arbitrary orientations, if desired.

This work was done by Jeffrey M. Oseas and Robert J. Calvel of Caltech for NASA's Jet Propulsion Laboratory. Further information is contained in a TSP [see page 1].
NPO-20795

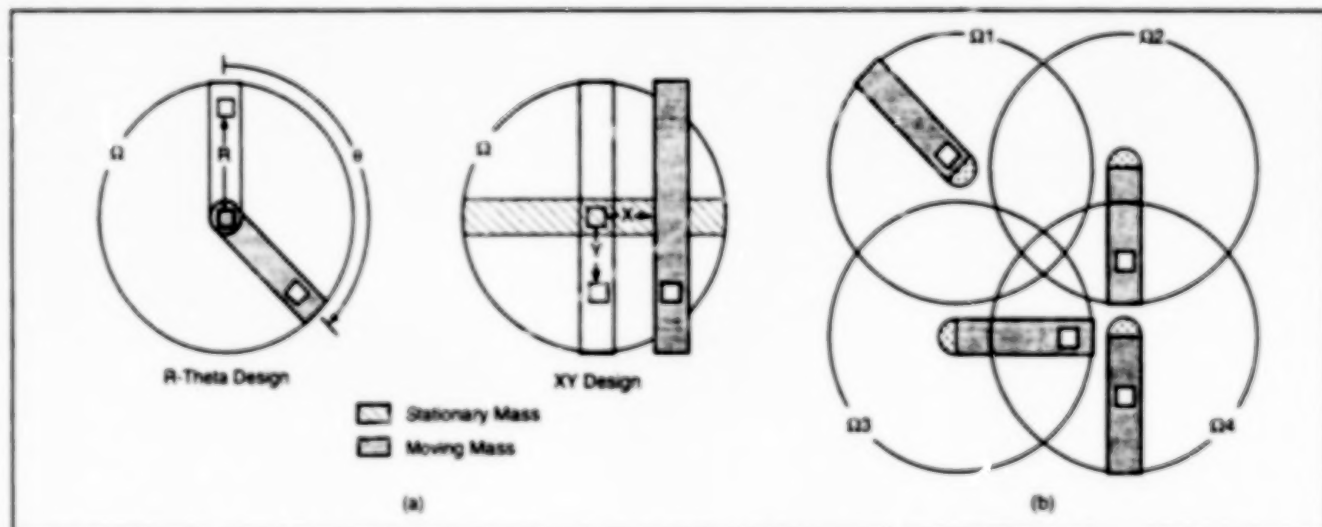


Figure 2. The Advantages of R-Theta to XY Goniometric Approaches are as follows: (a) The R-Theta design has a total mass of approximately 25 percent of the XY design and a moving mass of approximately 50 percent. These percentages will increase somewhat with the addition of a derotation stage to the R-Theta design and will also be a function of the exact stage designs. (b) In packaging of four R-Theta goniometers with overlapping fields-of-motion (where the four regions Ω all lay on the same spherical surface), the figure illustrates the ability to create significant overlaps in the regions to a degree impossible to achieve with conventional XY goniometric devices.



Machinery

Hardware, Techniques, and Processes

37 Multiple-DOF Surface-Acoustic-Wave Piezoelectric Motors

Multiple-DOF Surface-Acoustic-Wave Piezoelectric Motors

Motions in multiple DOFs could be controlled simultaneously.

NASA's Jet Propulsion Laboratory,
Pasadena, California

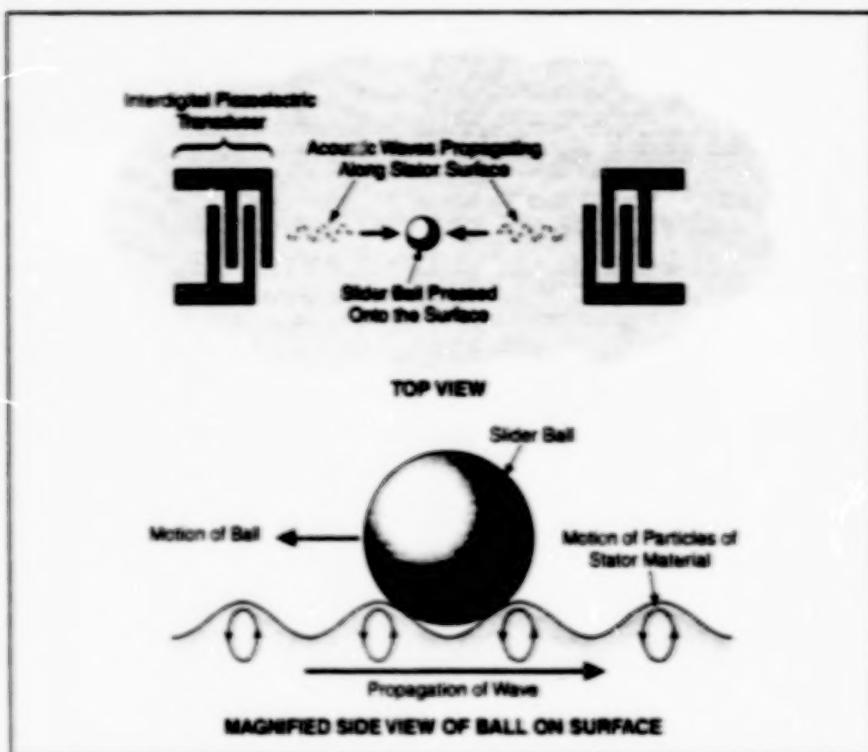


Figure 1. Surface Acoustic Waves are launched by suitably phased interdigital piezoelectric transducers at opposite ends of a stator. The slider ball rides the crests of the waves. Unlike in ocean surfing, the direction of motion of the ball is opposite the direction of propagation of the waves.

Surface-acoustic-wave (SAW) piezoelectric motors capable of operating in multiple degrees of freedom (DOFs) simultaneously have been proposed. A particularly useful motor of this type could provide both linear and rotary motions. Another particularly useful motor of this type would feature a spherical joint that could be made to undergo controlled, simultaneous rotations about two orthogonal axes; such a motor could serve as a compact actuator in a joint of a robot arm and could be constructed as an integral part of the arm.

Single-DOF SAW piezoelectric motors have been reported previously [for example, in "High-Torque Ultrasonic Motors" (NPO-19835), NASA Tech Briefs, Vol. 20, No. 10 (October 1996), page 12b]. Though the practical implementation can be fraught with difficulties, basic principle of operation in the single-DOF case is straightforward.

Piezoelectric transducer(s) excite waves that travel along the surface of a stator. A round object (e.g., a rod or a ball) in frictional contact with the stator rides the crests of the waves and is thereby made to move along the surface of the stator (see Figure 1). The resulting rotary or linear motion is coupled to an output shaft. The direction of motion (left or right in the example of Figure 1) is controlled by activating individual piezoelectric transducers. The speed increases with the amplitudes of the waves and thus with the magnitude of the voltage applied to the transducers.

Figure 2 depicts a simple example of a hemispherical motor that would tilt a shaft in two degrees of freedom. The shaft would be anchored in a spherical bearing nominally located at the center of the spherical coordinate system. A slider ball on the inner end of the shaft would make contact with the hemispherical surface,

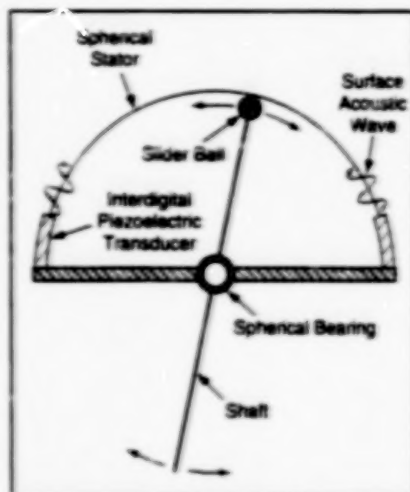


Figure 2. A Hemispherical Motor with two degrees of freedom would operate according to basic principle illustrated in Figure 1, and would take advantage of the fact that waves propagate along curved surfaces as well as along flat ones.

along which surface acoustic waves would be launched by two orthogonally located pairs of piezoelectric transducers (one pair for each degree of freedom). The bearing would be mounted in a plate connected to the hemispherical surface by use of screws, which would be adjusted to obtain the desired force of contact between the slider ball and the hemispherical surface.

This work was done by Yoseph Bar-Cohen of Caltech for NASA's Jet Propulsion Laboratory. Further information is contained in a TSP [see page 1].

In accordance with Public Law 96-517, the contractor has elected to retain title to this invention. Inquiries concerning rights for its commercial use should be addressed to

Technology Reporting Office

JPL

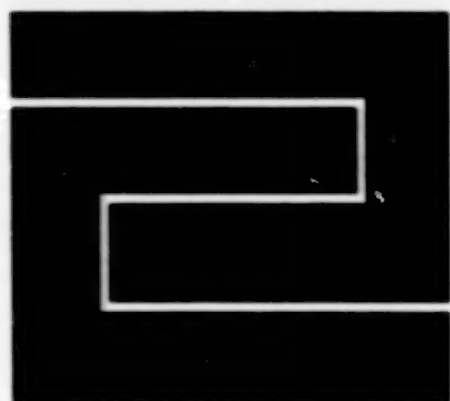
Mail Stop 122-116

4800 Oak Grove Drive

Pasadena, CA 91109

(818) 354-2240

Refer to NPO-20735, volume and number of this NASA Tech Briefs issue, and the page number.



Fabrication Technology

Hardware, Techniques, and Processes

41 *Manually Operated Weld-Filler-Wire Feeder*

Manually Operated Weld-Filler-Wire Feeder

This device is adaptable, its use is easy to learn, and it is relatively inexpensive.

A simple, manually operated mechanical device will ensure a smooth and predictable motion when feeding filler wire into a molten weld pool in gas tungsten arc welding (GTAW). This device simplifies and/or reduces the requirements for a dexterous hand to hold and manipulate filler wire. This device will grant, to the GTAW process, a level of consistency and integrity heretofore unknown.

At present, GTAW is performed manually by trained welders. The most common version of the GTAW process for aerospace-related hardware involves the addition of filler wire in a molten weld pool. The diameter of the filler wire can range from 1/64 to 3/16 in. (0.4 to 4.8 mm). Traditionally, a welder uses one hand to hold and/or manipulate a welding torch while manipulating the wire with the other hand. To ensure the consistency and integrity of a weld, a welder must feed the filler wire into the molten weld pool in a selective and specific fashion in coordination with manipulation of the torch. In other words, the repeatability and reliability of manual GTAW is tightly contingent on the human factor; that is, the welder's skill in manipulating a welding torch while simultaneously feeding filler wire into a molten weld pool. Clearly, the manual feeding of filler wire is a skill that requires physical dexterity (hand, finger, wrist) as well as precise hand/eye coordination. Not surprisingly, wide variations in hand, wrist, and finger movements have been observed from welder to welder and from time to time.

The present manually operated weld-filler-wire feeder is a means of reducing reliance on the welder's dexterity while increasing consistency and integrity. The wire feeder includes a metal frame with a knurled roller wheel mounted on a poly-

imide (VespelTM or TorlonTM) bushing that promotes low-friction movement. This roller is attached to the center of long axis of the metal frame. The frame ends are turned up as tabs perpendicular to the long axis where they protrude slightly above the top of the roller. Holes near the edge in each tab, are aligned with each other and are centered on the width of the roller. These holes are then positioned where the inside diameter of the roller is approximately tangent to a point central to the holes. On the side of the frame opposite the roller, a loop (ring) is attached tangentially to the frame with a rivet that allows the loop to rotate about its attachment point. The loop is there to assist the welder in holding the device.

A length of filler wire is threaded through the holes in the end tabs by the welder, who aligns the wire across the roller. A small amount of tension is needed to keep the wire in contact with the roller so that it remains fixed in the frame when tilted out of plane and thumb pressure is briefly released from the wire. Because too much tension can cause undue friction and impede the pushing of the wire across the roller, to accommodate wires of different diameters, the welder can bend the frame very slightly up or down to apply the right amount of pressure against the roller. The device is then lightly grasped in the hand normally used to hold wire. The welder's index or middle finger is placed through the loop, and the frame is moved to place the device in a comfortable position across the upper palm and lower portion of the fingers. The thumb is then brought over the top of the wire and placed so it can be moved from near the back of the frame, across the roller, and toward the front of the frame. The wire is thus fed through the

device at a steady rate to a predictable location; that is, in axial alignment with the holes and the roller.

In assuring a smooth, steady feeding of filler wire to a predictable location, this manually operated weld-filler-wire feeder advances the state of the art of GTAW. By overcoming the human-dexterity problems associated with manually feeding filler wire during GTAW, this device assures both consistency among welders and consistency between jobs performed by the same welder at different times. Because of its simplicity, the use of this device is easily learned, regardless of the user's previous skill or hand size. Because this device contains fewer parts than do other devices designed for the same purpose, it can be manufactured economically. Because it can be adapted to numerous filler wire diameters and can hold and manipulate multiple wires at the same time, its usefulness is assured across a broad spectrum. Of particular interest to the U.S. space program is the ability of this device to hold multiple wires simultaneously and thus to facilitate the welding of reactive alloys. An added benefit of this device is that it will keep wire clean by minimizing hand or glove contact. The device is expected to offer benefits wherever GTAW is performed — not only in the space program, but also in commercial settings.

This work was done by Daniel J. Rybicki of Lockheed Martin for Johnson Space Center.

This invention is owned by NASA, and a patent application has been filed. Inquiries concerning nonexclusive or exclusive license for its commercial development should be addressed to the Patent Counsel, Johnson Space Center, (281) 483-0837. Refer to MSC-23026.



Mathematics and Information Sciences

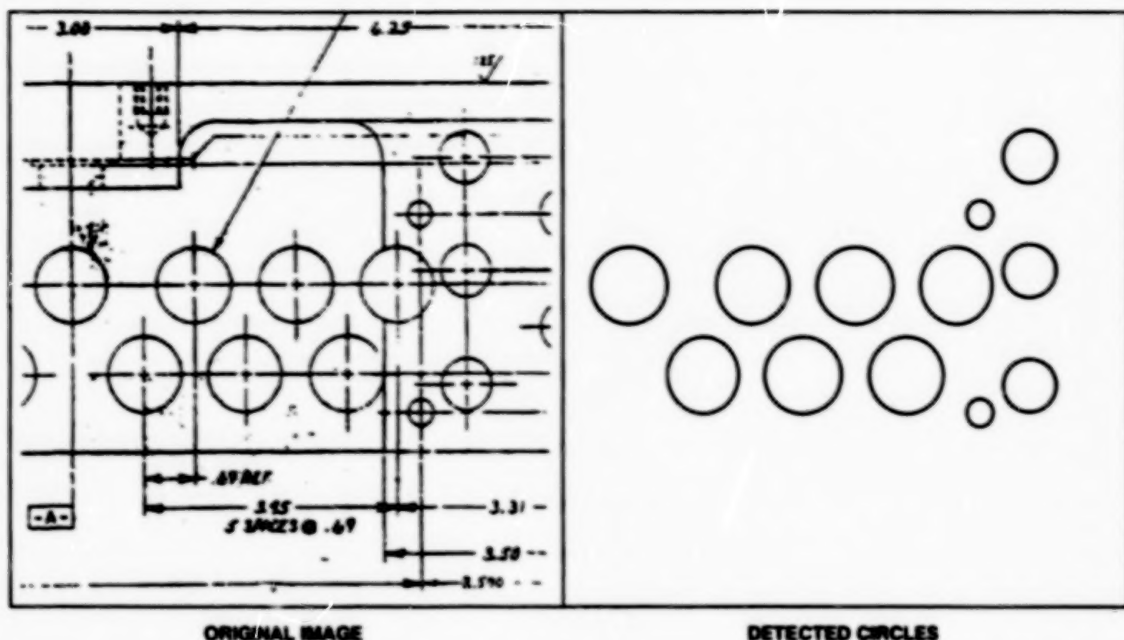
Hardware, Techniques, and Processes

- 45 Finding Known Shapes in an Image by Pruning Parameter Space
- 46 Digital Library of NACA Reports
- 46 RS Forward Error Correction for Variable-Length Frames
- 47 Fast NRZLM Encoding and Decoding Algorithm
- 48 Program for Controlling Digital Instrumentation Recorders

Finding Known Shapes in an Image by Pruning Parameter Space

This method is both efficient and robust.

NASA's Jet Propulsion Laboratory,
Pasadena, California



Circles in a Noisy Scanned Engineering Drawing were detected by processing the digitized scanned image according to the method described in the text.

An improved method of processing two- and three-dimensional image data to locate known shapes called "geometric primitives" involves (1) extraction of edges and other relevant image features and (2) performing a hierarchical search, in a space of parameters of equations that describe the shapes of the features, for those parameters that represent the geometric primitives. This method is inspired by prior object-recognition methods in which parameter spaces are recursively divided and pruned. The most closely related prior methods of this type are based on variations of the Hough transform. Whereas the prior methods have generally offered robustness or computational efficiency but not both, this method offers both, along with other advantages: It enables the efficient and robust extraction of geometric primitives from noisy and incomplete data that include many distracting data, without need for initial estimates of the locations of the geometric primitives.

In this method, one extracts geometric primitives from image data in the following way: One searches for parameters that satisfy a quantitative acceptance criterion based on the number of data features that approximate geometric primitives within a specified error measure. The search involves the subdivision of the parameter

space into rectilinear cells, possibly starting from one or a few large cell(s). Each point in the parameter space represents a candidate position of a geometric primitive in the data. The cells are volumes of the parameter space and thus represent continuous ranges of locations of geometric primitives in the parameter space.

Each cell in the parameter space is tested to determine whether it can contain the parameters of a primitive that satisfies the acceptance criterion. If the acceptance criterion is not satisfied, the cell is pruned. If the acceptance criterion is satisfied, then the cell is split into two subcells and the subcells are examined recursively. When the smallest specified cell size is reached, the primitive at the center of the cell is tested to determine whether it meets the acceptance criterion.

At each state in this recursive process of division and pruning, the test is performed by an efficient algorithm that is conservative in that it never rules out a cell that contains a good primitive. Although this test can sometimes fail to rule out a cell that does not contain any good primitive, this failure does not result in false positives in the end because false positives are ruled out in the subsequent tests performed at subsequent finer subdivisions.

An interesting facet of this method is that

a hierarchy is constructed not only in the parameter space, but also in the image feature space. This makes it possible for many image features to be pruned at each step with little computation, in addition to the pruning in the parameter space. Empirical evidence suggests that this hierarchical pruning reduces the complexity of the extraction process. In cases in which the number of data greatly exceed that needed for extraction of geometric primitives, robust random sampling can also be used to increase speed.

In some initial test cases, the geometric primitives were relatively simple shapes (circles and cylinders). The test cases were representative of three different image-recognition problems: identifying craters in digital images of planetary bodies, detecting the predominantly cylindrical bodies of unexploded bombs in images of a military test range, and detecting circles in an engineering drawing (see figure). Examples of other potential applications include locating parts for robotic assembly and detecting symbols in engineering drawings for transcription by computer.

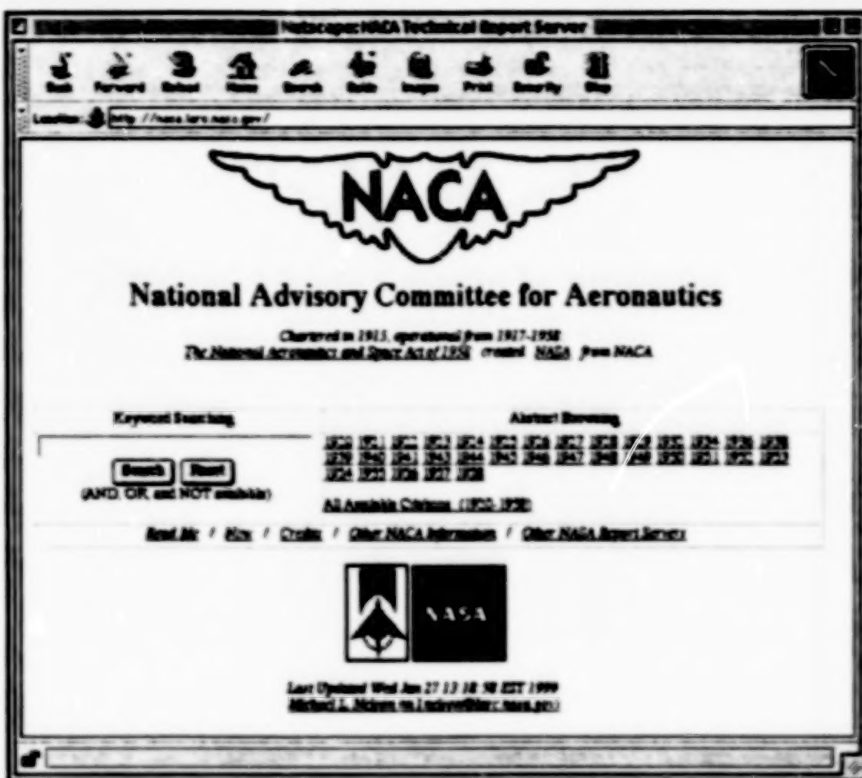
This work was done by Clark F. Olson of Caltech for NASA's Jet Propulsion Laboratory. Further information is contained in a TSP [see page 1].

NPO-20941

Digital Library of NACA Reports

Aging paper NACA documents are scanned, then disseminated in electronic form.

Langley Research Center,
Hampton, Virginia



The Home Page of the NACATRS provides access for browsing and keyword searching of NACA reports.

The NACA Technical Report Server (NACATRS) is both a node in the NASA Technical Report Server and a stand-alone World Wide Web (WWW) site. The NACATRS is dedicated to the preservation and dissemination of reports produced by the National Advisory Committee for Aeronautics (NACA).

NACA, which evolved into the predecessor to NASA, existed from 1915 until 1958. The main product of NACA's research is a multi-tiered series of reports, the number of which is estimated to be between 20,000 and 30,000. These reports — especially

the ones that address issues of general aviation and the fundamentals of flight — remain in high demand. Although significant collections of NACA documents exist at a handful of NASA centers, universities, and government and industrial research laboratories, no single library contains a complete collection. Furthermore, because of their age, high circulation, and acid-based paper, many of these reports are in poor condition and will cease to be serviceable in the near future. Conversion to digital form is necessary for preservation and for wider dissemination.

At present, the NACATRS collection contains about 2,300 documents, and is growing at rate of about 30 documents per week. Each NACA document is electronically scanned, generating image data in Tagged Image/Interchange File Format (TIFF). Optical Character Recognition (OCR) is not performed, primarily because NACA publications contain numerous pages of equations, tables, charts, and figures, none of which are well suited for OCR. Instead, the document is converted into a combination of Graphics Interchange Format (GIF) and Portable Document Format (PDF) files for easier dissemination via the WWW.

The NACATRS offers browsing and keyword searching of its holdings (see figure). Reports are also accessible via the following naming convention: <http://naca.larc.nasa.gov/reports/YEAR/naca-reportTYPE-NUMBER>. For example, the popular NACA Report 1135 is available at <http://naca.larc.nasa.gov/reports/1953/naca-report-1135/>. Once a report has been retrieved, it is initially presented in the form of thumbnail images of pages. Clicking on a thumbnail image results in presentation of a large GIF version of the image for easy on-line viewing. As many as ten thumbnail images can be shown at a time, with such options as "next," "previous," "first," and "last" for switching among pages of a large report. Similar options are available for viewing single GIF page images. The user can download the entire report as a single PDF file.

This program was written by Michael L. Nelson of Langley Research Center. Further information is contained in a TSP [see page 1].
L-17844

RS Forward Error Correction for Variable-Length Frames

Method accommodates dynamically varying frame length.

Goddard Space Flight Center,
Greenbelt, Maryland

A method of forward error correction by Reed-Solomon (RS) coding has been devised to increase the link margins of data-communication systems that must handle variable-length frames or packets of data. Heretofore, RS coding has involved fixed-length blocks: In order to encode variable-length frames, it has been necessary to (a)

choose a fixed block length equal to a multiple of some given block length and greater than or equal to the length of the longest variable-length frame and (b) in the case of a frame shorter than the fixed block length, pad or fill the remainder of the block with extra bytes. This is very inefficient because the fill conveys no useful information, and

any errors in the fill diminish the overall coding gain by using up some or all of the available error-correction capacity.

The present method accommodates dynamically varying frame length by use of equations that relate the frame length to a quantity known as the virtual-fill parameter. The concept of virtual fill (see fig-

ure) is not new; what is new here is the way in which virtual fill is used. In the traditional fixed-length-block approach, all of the code parameters, including the virtual-fill parameter and the frame length, are set in advance or initialized at startup time and are not changed during the encoding/decoding process. In the present method, the virtual-fill parameter and the frame length are allowed to vary while the other parameters are held constant.

Let

m = the number of bits per symbol
 $n = 2^{m-1}$ total number of symbols per code block

t = number of correctable errors

VF = number of virtual fill symbols (≥ 0)

I = interleaving parameter (≥ 1)

FL = total frame length [number of data + parity (check) symbols]

$FSPL$ = frame-synchronization-pattern length

DFL = length of (number of symbols in) the data field in a code block

CBL = number of data plus parity (check) symbols in a code block.

Then the basic equations for the RS code parameters are the following:

$$(1) FL = FSPL + (n - 2t - VF) + 2t,$$

$$(2) DFL = n - 2t - VF, \text{ and}$$

$$(3) CBL = n - VF.$$

Straightforward algebraic manipulation of the foregoing equations yields:

$$(4) DFL = (FL - FSPL)/I - 2t \text{ and}$$

$$(5) VF = n - (FL - FSPL)/I.$$

Equation 4 is used in the RS encoder because DFL is a parameter of the encoding algorithm. Equation 5 is used to dynamically obtain the virtual fill length for a given frame based on its length. In both the encoder and decoder, the limit check on valid frame length is given by

$$(6) FSPL + 2tI \leq FL \leq FSPL + nI.$$

These equations can readily be incorporated into a software implementation and conceivably also into a hardware implementation of the RS encoder and decoder, provided that the encoder and decoder

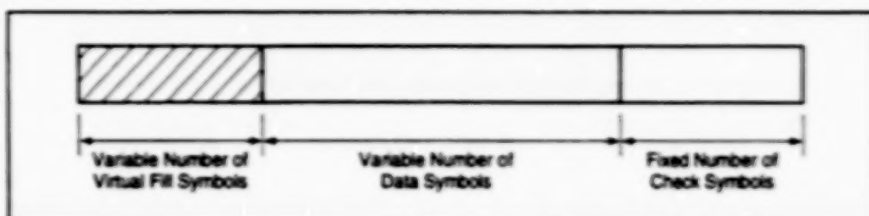
can each act individually to determine the length of the current frame.

Even in a system in which data are generated in fixed-length frames, it could be advantageous to dynamically vary FL , in response to the bit-error rate, to optimize the forward-error-correction capability. In general, the number of check symbols per code block and the coding gain increase as FL decreases. The disadvantage of this method is that proportions of overhead are greater for smaller packets.

This work was done by Steve Duran of Goddard Space Flight Center.

Further information is contained in a TSP [see page 1].

GSC-13916



Virtual Fill Symbols conceptually occupy the portion of a code block not occupied by a data frame shorter than the longest allowable frame. Unlike pad or real fill symbols in the traditional approach, virtual fill symbols are not transmitted. In the present method, the number of virtual fill symbols is varied dynamically to compensate for variable frame length.

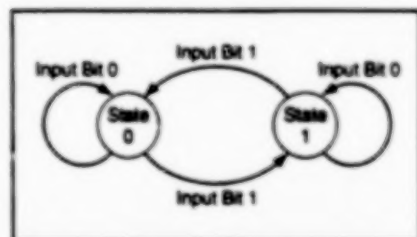
Fast NRZLM Encoding and Decoding Algorithm

Byte-oriented algorithms save time.

A recently developed algorithm saves encoding and decoding time in the operation of data-communication systems that utilize the NRZM code, which is derived from the better-known non-return-to-zero-level (NRZL) code. This algorithm utilizes lookup tables that contain the results of routine encoding and decoding computations that would otherwise have to be performed repeatedly.

A stream of symbols in NRZM code is generated from an input stream of symbols in NRZL code. The NRZM code was originally developed as a means to convert a steady, high-level signal (a long sequence of 1111...111) into a variable signal (1010...10 or 0101...01, depending on the choice of 0 or 1 for the initial state of the coding algorithm). The NRZM code provides signal-level transitions in an idle state when there is time for synchronization of encoding and decoding equipment.

An explanation of the nomenclature of algorithms for NRZM encoding and decoding is prerequisite to an explanation of the present innovative algorithm. In general, algorithms that transform streams of sym-



A Two-State Automaton that makes transitions in response to an input bit of 1 implements the NRZM code and the Binary NRZM algorithm.

bits between NRZL and NRZM codes are denoted collectively as "NRZLM" algorithms. Of these, subalgorithms that transform NRZL input streams into NRZM output streams are called "NRZM" algorithms, while subalgorithms that transform NRZM input streams into NRZL output streams are called "NRZL" algorithms.

Before the present innovative NRZM algorithm was developed, transformations between NRZL and NRZM were effected by the Binary NRZLM algorithm, which is bit-oriented; that is, it operates on only one bit at a time. Even if an NRZL data

source is byte-oriented, it is necessary to disassemble the NRZL bytes into bits, then encode the bits into NRZM one at a time by use of the Binary NRZM algorithm, then reassemble the NRZM-encoded bits into bytes. Similar considerations apply to use of the Binary NRZL algorithm to decode from NRZM back to NRZL.

The NRZM code and the Binary NRZM algorithm can be explained in terms of a finite-state automaton that can be in either of two states; 0 or 1 (see figure). These states correspond to output bits. If the automaton is in either state and receives an input bit 0, it remains in that state. If the automaton is in either state and receives an input bit of 1, it changes to the other state. Thus, the output bit for a given input bit depends on the state of the decoder after receipt of the immediately preceding input bit; this state is called the "last state." The last state depends on the chosen initial state and on the sequence of input bits up through the immediately preceding bit.

Thus, in the Binary NRZM algorithm, it is necessary to go bit-by-bit through the entire sequence of preceding NRZL input

Goddard Space Flight Center,
 Greenbelt, Maryland

bits to arrive at the output NRZM bit for a given input NRZL bit. Similarly, in the Binary NRZL algorithm, it is necessary to go bit-by-bit through the entire sequence of preceding NRZM input bits to arrive at the NRZL output bit for a given input NRZM bit.

The present innovative NRZLM algorithm is byte-oriented. It exploits the following observation: One can commence coding or decoding from any point in a sequence of input bits, without having to step through the entire sequence of preceding input bits, provided that one has some other way of knowing the last state

immediately preceding that point. Thus, if bits in an input sequence are grouped into bytes, one can start to encode or decode at the beginning of any byte, provided that one knows the last state produced by the preceding byte or bytes.

In formulating this byte-oriented NRZLM algorithm, the results of coding and decoding operations are precomputed by the Binary NRZM and Binary NRZL algorithms and stored in lookup tables; these tables contain the output bytes and last states for all possible input bytes and preceding last states. Thus,

instead of a long sequence of operations on individual bits, the encoding and decoding of each input byte involves only initialization by use of the last state from the preceding byte, followed by a table-lookup operation to find the output byte and another table-lookup operation to find the new last state.

This work was done by Samion Kizhner and Timothy Ray of Goddard Space Flight Center. Further information is contained in a TSP [see page 1].

GSC-13825

Program for Controlling Digital Instrumentation Recorders

A computer program enables the simultaneous monitoring and control of two commercial digital instrumentation recorders, each comprising a variable-rate buffer and a data tape recorder. The program can issue all standard tape-motion-related commands (fast forward, rewind, record, forward, reverse, and eject) plus commands for tape search, time code, and buffer settings. The program provides a graphical user interface

that facilitates control by the user and displays the operational statuses of the buffers and tape recorders. The program generates a log file that includes a time and date stamp for each control command sent to, and response received from, each buffer and recorder. An option exists in the program to produce tape copies by dubbing from one recorder to the other. The program can also be used to effect a procedure in which data are

recorded first on one tape recorder, then the other tape recorder is brought into operation shortly before the end of first tape, so that there is some overlap to ensure continuous recording during a long recording session.

This work was done by Danny B. Sylvester and David M. Weihe of The Boeing Company for Kennedy Space Center.

KSC-12005



END

11-14-02